

Dynamics of multiple protoplanets embedded in gas/pebble disks and its dependence on Σ and ν parameters

M. Brož¹, O. Chrenko¹, D. Nesvorný², M. Lambrechts³

¹ Institute of Astronomy, Charles University, Prague, V Holešovičkách 2, 18000 Prague 8, Czech Republic,
e-mail: mira@sirrah.troja.mff.cuni.cz

² Department of Space Studies, Southwest Research Institute, 1050 Walnut St., Suite 300, Boulder, CO 80302, USA

³ Lund Observatory, Department of Astronomy and Theoretical Physics, Lund University, Box 43, 22100 Lund, Sweden

Received ???; accepted ???

ABSTRACT

Protoplanets of Super-Earth sizes may get trapped in convergence zones for planetary migration and form gas giants there. These growing planets undergo accretion heating, which triggers a hot-trail effect that can reverse migration directions, increase planetary eccentricities and prevent resonant captures of migrating planets (Chrenko et al. 2017). In this work, we study populations of embryos accreting pebbles, under different conditions, by changing the surface density, viscosity, pebble flux, mass, and the number of protoplanets. For modelling we use FARGO-THORIN 2D hydrocode which incorporates a pebble disk as a 2nd pressure-less fluid, the coupling between the gas and pebbles and the flux-limited diffusion approximation for radiative transfer.

We find that massive embryos embedded in a disk with high surface density ($\Sigma = 990 \text{ g cm}^{-2}$ at 5.2 au) undergo numerous ‘unsuccessful’ two-body encounters which do not lead to a merger. Only when a 3rd protoplanet arrives to the convergence zone, three-body encounters lead to mergers. For a low-viscosity disk ($\nu = 5 \times 10^{13} \text{ cm}^2 \text{ s}^{-1}$) a massive coorbital is a possible outcome, for which a pebble isolation develops and the coorbital is further stabilised. For more massive protoplanets ($5 M_{\oplus}$), the convergence radius is located further out, in the ice-giant zone. After a series of encounters, there is an evolution driven by a dynamical torque of a tadpole region, which is systematically repeated several times, until the coorbital configuration is disrupted and planets merge. This may be a pathway how to solve the problem that coorbitals often form in simulations but they are not observed in nature.

In contrast, the joint evolution of 120 low-mass protoplanets ($0.1 M_{\oplus}$) reveals completely different dynamics. The evolution is no longer smooth, but rather a random walk. This is because the spiral arms, developed in the gas disk due to Lindblad resonances, overlap with each other and affect not only a single protoplanet but several in the surroundings. Our hydrodynamical simulations may have important implications for N-body simulations of planetary migration that use simplified torque prescriptions and are thus unable to capture protoplanet dynamics in its full glory.

Key words. hydrodynamics – protoplanetary disks – planet-disk interactions – planets and satellites: formation

1. Introduction

A giant planet core formation is a key to understand the evolution of the Solar System, and exoplanetary systems as well. It is believed that gas giants, and possibly (some subset of) the super-Earths, form in a special region of the protoplanetary disk where an opacity transition (snowline) is located, and a transition between the viscously-heated and irradiated (flared) parts creates a suitable convergence zone (Bitsch et al. 2014). A relatively massive solid core of about 10 to $20 M_{\oplus}$ is then needed to accrete the surrounding gas (Pollack et al. 1996), before the disk dispersal. Consequently, there is an ongoing ‘quest’ for the fastest mechanism which would beat other (slower) mechanisms of core formation. At the same time, it is necessary to address the gas flow which determines the actual critical mass. A number of processes were already discovered which contribute either in a positive way, e.g. the pebble accretion due to an aerodynamic drag in the respective Hill spheres (Lambrechts & Johansen 2012), or a negative way, e.g. the concurrent inflow and outflow in advective atmospheres (Lambrechts & Lega 2017).

In our previous paper (Chrenko et al. 2017), we studied yet another process called the hot-trail effect which arises naturally due to the heat liberated by the accretion of pebbles onto protoplanets with several Earth masses. This heat expands the gas be-

hind the protoplanet, creating an underdense region and changing the gravitational torque of gas acting on the protoplanet. In our setup, we simply assumed that the protoplanets radiate the accretion energy and heat the surrounding gas; there is no blanketing by the atmosphere, or a magma ocean which would keep the heat within the protoplanets. We used a self-consistent 2D model with interacting gas and pebble disks (see below), so the pebble flux onto a given protoplanet is not simply prescribed. As a result, the migration rates of protoplanets (or equivalently the torques) are altered (Benítez-Llambay et al. 2015), and their eccentricities increase substantially. These non-zero eccentricities ‘change the game’, because the captures in mean-motion resonances between protoplanets are then much less probable.

Eklund & Masset (2017) used a 3D model to study a dependence of the hot trail on the initial values of the eccentricity e_0 , inclination i_0 , the protoplanet mass M_{em} , and the accretion rate \dot{M} , which was prescribed in their model. It turns out that asymptotic values of the eccentricity e_{asy} (or i_{asy}) are important for the dynamics, probably more than de/dt , di/dt . They also realized the inclination can remain low ($< 10^{-4}$ rad) – if its initial value was very low – because even a moderate eccentricity suppresses a further increase of i . As a consequence, 2D models in which no vertical hot trail is present may be still a viable and less expensive alternative. Nevertheless, we shall keep track of

orbital inclinations excited by mutual encounters, because they do affect the rate of pebble accretion when the protoplanets orbit above or below the pebble disk (Levison et al. 2015).

Given the expensiveness of hydrodynamical computations, we considered a single set of parameters in Chrenko et al. (2017), although the dependence on disk(s) parameters is crucial. In particular, different values of the surface density Σ , the pebble flux \dot{M}_p , or the viscosity ν can potentially lead to very different outcomes. One should also vary protoplanet masses M_{em} , their numbers, or their initial spacing in terms of the mutual Hill radius, because the dynamics is controlled not only by properties of *individual* protoplanets (disk-driven migration rates, etc.), but also by mutual interactions within the whole system. Consequently, the main goal of this paper is to study the evolution of multiple planets embedded in gas/pebble disks and its dependence on parameters.

Knowing the correct migration rates, damping and pumping of e 's and i 's, is also important for non-hydrodynamic models. For example Coleman & Nelson (2016) or Izidoro et al. (2017) used an N-body model with parametrized migration rates to explain configurations of compact Kepler planetary systems. In their case all bodies of a given size drift in a systematic way, because the disk torques were estimated for single planets, and no heating torque was included. Hereinafter, we shall see the situation is actually more complicated.

Our paper is organized as follows. In Section 2 we describe the radiation-hydrodynamical model and its common parameters. In Section 3 we present results of 8 different simulations, including detailed views of protoplanet encounters. Section 4 is devoted to conclusions. A broader context of our work is discussed in Appendix C.

2. Model

Our 2D numerical model is based on FARGO (Masset 2000), and was described in detail in Chrenko et al. (2017).¹ Nevertheless, in order to present a self-contained paper we recall the system of radiation–hydrodynamic equations (i.e. the continuity, Navier–Stokes, energy, continuity of pebbles, momentum of pebbles, equation of state, and gravity on protoplanets) and our notation here:

$$\frac{\partial \Sigma}{\partial t} + \mathbf{v} \cdot \nabla \Sigma = -\Sigma \nabla \cdot \mathbf{v} - \left(\frac{\partial \Sigma}{\partial t} \right)_{acc}, \quad (1)$$

$$\frac{\partial \mathbf{v}}{\partial t} + \mathbf{v} \cdot \nabla \mathbf{v} = -\frac{1}{\Sigma} \nabla P + \frac{1}{\Sigma} \nabla \cdot \mathbf{T} - \frac{\int \rho \nabla \phi \, dz}{\Sigma} + \frac{\Sigma_p \Omega_K}{\Sigma} (\mathbf{u} - \mathbf{v}), \quad (2)$$

$$\begin{aligned} \frac{\partial E}{\partial t} + \mathbf{v} \cdot \nabla E = & -E \nabla \cdot \mathbf{v} - P \nabla \cdot \mathbf{v} + Q_{visc} + \frac{2\sigma T_{irr}^4}{\tau_{eff}} - \frac{2\sigma T^4}{\tau_{eff}} + \\ & + 2H \nabla \cdot \frac{16\sigma \lambda_{lim}}{\rho_0 \kappa_R} T^3 \nabla T + \sum_i \frac{GM_i \dot{M}_i}{R_i S_{cell}} \delta(\mathbf{r}_i), \quad (3) \end{aligned}$$

$$\frac{\partial \Sigma_p}{\partial t} + \mathbf{u} \cdot \nabla \Sigma_p = -\Sigma_p \nabla \cdot \mathbf{u} - \left(\frac{\partial \Sigma_p}{\partial t} \right)_{acc}, \quad (4)$$

$$\frac{\partial \mathbf{u}}{\partial t} + \mathbf{u} \cdot \nabla \mathbf{u} = -\frac{\int \rho_p \nabla \phi \, dz}{\Sigma_p} - \frac{\Omega_K}{\tau} (\mathbf{u} - \mathbf{v}), \quad (5)$$

$$P = \Sigma \frac{RT}{\mu} = (\gamma - 1)E, \quad (6)$$

$$\begin{aligned} \ddot{\mathbf{r}}_i = & -\frac{GM_\star}{r_i^3} \mathbf{r}_i - \sum_{j \neq i} \frac{GM_j}{|\mathbf{r}_i - \mathbf{r}_j|^3} (\mathbf{r}_i - \mathbf{r}_j) - \\ & - \iint \frac{G\Sigma}{|\mathbf{r}_i - \mathbf{r}_{cell}|^3} (\mathbf{r}_i - \mathbf{r}_{cell}) r d\theta dr + f_z \hat{z} \quad \text{for } \forall i, \quad (7) \end{aligned}$$

where Σ denotes the gas surface density, \mathbf{v} gas velocity, $(\partial \Sigma / \partial t)_{acc}$ gas accretion term, P vertically integrated pressure, \mathbf{T} viscous stress tensor, ρ gas volumetric density, ϕ gravitational potential of the Sun and protoplanets, with a cubic smoothing due to a finite cell size (Klahr & Kley 2006), z vertical coordinate, Σ_p pebble surface density, \mathbf{u} pebble velocity, $(\partial \Sigma_p / \partial t)_{acc}$ pebble accretion term for both Bondi and Hill regimes (detailed in Chrenko et al. 2017), Ω_K the Keplerian angular velocity, τ the Stokes number of pebbles, always assuming the Epstein drag regime, E gas internal energy, Q_{visc} viscous heating term (Mihalas & Weibel Mihalas 1984), σ the Stefan–Boltzmann constant, T_{irr} irradiation temperature (Chiang & Goldreich 1997), τ_{eff} effective optical depth (Hubený 1990), T gas temperature, H vertical (pressure) scale height, λ_{lim} flux limiter (Kley 1989), ρ_0 midplane density, κ_R the Rosseland opacity (the Planck opacity κ_P hidden in τ_{eff} is assumed the same), G gravitational constant, M_i protoplanet mass, R_i protoplanet radius, S_{cell} cell area in which it is located, μ mean molecular weight, γ adiabatic index, $\ddot{\mathbf{r}}_i$ gravitational acceleration of the body i , where a smoothing is applied again for the 3rd term; and f_z vertical damping prescription (Tanaka & Ward 2004).

More specifically, we use the following smoothing of the potential:

$$\phi_i(d) = \begin{cases} -\frac{GM_i}{d} & \text{for } d > r_{sm}, \\ -\frac{GM_i}{d} \left[\left(\frac{d}{r_{sm}} \right)^4 - 2 \left(\frac{d}{r_{sm}} \right)^3 + 2 \frac{d}{r_{sm}} \right] & \text{for } d \leq r_{sm}, \end{cases} \quad (8)$$

with the smoothing length $r_{sm} = 0.5R_H$, where R_H denotes the Hill radius of the respective protoplanet. We still integrate in the vertical direction over the density profile:

$$\rho(z) = \frac{\Sigma}{\sqrt{2\pi}H} \exp\left(-\frac{z^2}{2H^2}\right) \quad (9)$$

to avoid a smoothing over H (Müller et al. 2012).

We performed a few modifications of the code, namely we improved the successive over-relaxation (SOR) solver for the radiative step, so that iterations stop when the system of equations is fulfilled at the machine precision. We also included the gas accretion term using Kley (1999) prescription with f_{acc} parameter, even though it is switched off in most simulations. Bell & Lin (1994) LTE opacities were implemented more carefully without even minor jumps at the transitions.

The nominal simulation presented in Chrenko et al. (2017), hereinafter called `CaseIII_nominal`, had the following parameters: the gas surface density $\Sigma_0 = 750 \text{ g cm}^{-2}$ at 1 au, slope $r^{-0.5}$, the aspect ratio $h = H/r$ and flaring are given by radiation processes during the relaxation phase (one can start with an arbitrary value, $h = 0.02$ or 0.10 , and the relaxation will converge to the same disk structure); adiabatic index $\gamma = 1.4$, molecular weight $\mu = 2.4 \text{ g mol}^{-1}$, vertical opacity drop $c_\kappa = 0.6$, effective temperature $T_\star = 4370 \text{ K}$, stellar radius $R_\star = 1.5 R_\odot$, disc albedo $A = 0.5$, softening parameter is $0.5R_H$, the entire Hill sphere is considered when calculating disk \leftrightarrow planet interactions, the inner boundary is $r_{min} = 2.8 \text{ au}$, outer boundary $r_{max} = 14 \text{ au}$, a damping BC (e.g. Kley & Dirksen 2006) is used to prevent spurious reflections, and applied up to $1.2r_{min}$ and from $0.9r_{max}$ on; quantities are damped towards their initial values, only during the relaxation phase the damping is towards zero radial velocity; the vertical damping parameter is 0.3 ,

¹ See also <http://sirrah.troja.mff.cuni.cz/~chrenko/>.

pebble flux $\dot{M}_p = 2 \times 10^{-4} M_\oplus \text{ yr}^{-1}$, turbulent stirring parameter $\alpha_p = 10^{-4}$, the Schmidt number $Sc = 1$, pebble coagulation efficiency $\epsilon_p = 0.5$, pebble bulk density $\rho_p = 1 \text{ g cm}^{-3}$, embryo density $\rho_{em} = 3 \text{ g cm}^{-3}$ (constant), embryo mass $M_{em} = 3.0 M_\oplus$, and their number $N_{em} = 4$.

For simplicity, we used a constant kinematic viscosity $\nu = 5.0 \times 10^{14} \text{ cm}^2 \text{ s}^{-1} \doteq 10^{-5}$ [c.u.], but we do not expect a drastic change when we would use an α -viscosity, with $\nu = \alpha c_s H$, where c_s denotes the (local) sound speed and H the scale height (Shakura & Sunyaev 1973). The viscously-heated region is actually from 3 to 7 au in our nominal model, the rest is irradiated. We also do not expect (prescribe) any jumps in viscosity due to MRI/dead regions, as our disk is cold throughout.

There are several limitations of our model we shall keep in mind. We do not account for the Stokes drag (i.e. pebble sizes D_p larger than the mean-free path ℓ), a reduction factor of the accretion rate needed for $\tau \gg 1$ (Ormel & Klahr 2010; Ida et al. 2016), or the gravity of pebbles (as emphasized by Benítez-Llambay & Pessah 2018). Nevertheless, our gas/pebble disks should be well within the respective limits. We find our typical pebble-to-gas ratio to be approximately 0.001, and if assume for the moment that the results of Benítez-Llambay & Pessah (2018) are applicable even in our more complicated case (i.e. non-fixed planets, eccentric orbits, with pebble accretion, back-reaction), the ratio of torques should be $\Gamma_p/\Gamma_g \doteq 0.05$. The pebble torque can thus be safely ignored for our disc conditions.

The discretisation in space we normally use is 1024×1536 cells in the radial and azimuthal directions. See Appendix A for an additional convergence test. The discretisation in time is controlled by the CFL condition; the maximal time step is $\Delta t = 3.725$ [c.u.] = $1/20 P_{orb}$ at 5.2 au. Orbital elements are output every $20 \Delta t$, and hydrodynamical fields every $500 \Delta t$. The nominal time span is approximately 50 kyr, but the simulations are prolonged whenever needed. The relative precision of the IAS15 integrator (Rein & Spiegel 2015) used for the planetary bodies is set to 10^{-9} .

3. Results

Apart from the nominal case, we performed 8 simulations which are summarised in Table 1. We always change one parameter (or two at most) and analyze how the overall evolution changes. The dependence on the gas surface density Σ , pebble flux \dot{M}_p , viscosity ν , embryo mass M_{em} , or their number N_{em} is a very basic question, indeed. We thus shall describe all of them (not-so-interesting included), with the most interesting implications discussed later in Section 4.

A very useful tool would be a construction of a complete Type-I migration map, i.e. a dependence of the torque Γ on the disk profiles $\Sigma(r)$, $T(r)$, the protoplanet mass M_{em} , and other parameters, in a similar way as in Paardekooper et al. (2011); Bitsch et al. (2013). In our case we have an additional parameter, namely the pebble flux \dot{M}_p , which makes this task more difficult though. It may also vary with the Stokes number τ (cf. Benítez-Llambay & Pessah 2018). At the same time, we would need an eccentricity excitation map, for the derivatives \dot{e} , and also for the asymptotic values e_{asy} . As we shall see in the next Sections, the situation is even worse, because there are mutual (hydrodynamical) interactions between the protoplanets too.

Table 1. Selected parameters of our hydrodynamical simulations, where Σ_0 denotes the gas surface density at 1 au, \dot{M}_p the pebble flux, ν the kinematic viscosity, M_{em} the embryos' mass, and N_{em} their number. For other parameters see the main text.

simulation	parameters
CaseIII_nominal	$\Sigma_0 = 750 \text{ g cm}^{-2}$ at 1 au, $\dot{M}_p = 2 \times 10^{-4} M_\oplus \text{ yr}^{-1}$, $\nu = 5.0 \times 10^{14} \text{ cm}^2 \text{ s}^{-1} \doteq 10^{-5}$ [c.u.], $M_{em} = 3.0 M_\oplus$, $N_{em} = 4$, $f_{acc} = 0$
Sigma_3times	$\Sigma_0 = 2250 \text{ g cm}^{-2}$
Sigma_1over3	$\Sigma_0 = 250 \text{ g cm}^{-2}$
pebbleflux_2e-5	$\dot{M}_p = 2 \times 10^{-5} M_\oplus \text{ yr}^{-1}$
viscosity_1e-6	$\nu = 5.0 \times 10^{13} \text{ cm}^2 \text{ s}^{-1} \doteq 10^{-6}$ [c.u.]
gasaccretion_1e-6	$f_{acc} = 10^{-6}$
totmass_20ME	$M_{em} = 5.0 M_\oplus$, $\dot{M}_p = 2 \times 10^{-5} M_\oplus \text{ yr}^{-1}$
embryos_1.5ME_8	$M_{em} = 1.5 M_\oplus$, $N_{em} = 8$
embryos_0.1ME_120	$M_{em} = 0.1 M_\oplus$, $N_{em} = 120$

3.1. Initial profiles

The initial radial profiles of the gas disk are shown in Figure 1. They were obtained by a relaxation procedure, prior to the simulation itself. The initial azimuthal profiles are uniform. Several simulations actually use the same gas disk as the nominal case, namely `pebbleflux_2e-5`, `embryos_1.5ME_8`, and `gasaccretion_1e-6`. Another two are only extensions of the nominal case towards larger radii, namely `embryos_0.1ME_120` to 16 au, and `totmass_20ME` from 8 to 40 au, because it turned out the convergence zone is located in the outer disk. The profiles of the pebble disk are shown in Figure B.1 for comparison. We assume the corresponding Stokes numbers τ are drift-limited and that initially the pebble flux \dot{M}_p is independent of the radial distance.

Classically, we would expect a convergence zone somewhere between the region driven by viscous heating, and irradiation (flaring). This is no longer true when we include the pebble accretion heating too. Coincidentally, profiles for `Sigma_1over3`, and `viscosity_1e-6` are very similar, but the disk dynamics is naturally different.

A global structure of the gas and pebble disks is shown in Figure 2. Initially, they are very smooth but after mere hundred orbital periods spiral arms in the gas disk are developed, surroundings of each protoplanet and its corotation region is affected by the accretion heating, and also accretion-related structures occur in the pebble disk.

3.2. Nominal case

Let us start with a **warning**: for substantially non-Keplerian orbits, it is rather important to plot the radial distance r instead of a , q , Q (the semimajor axis, pericentre, and apocentre). For example a spiral orbit has a perfectly smooth $r(t)$, with no oscillations whatsoever, but its eccentricity $e \gg 0$. One could be misled by non-zero e and think of close encounters between such orbits, but in fact there is always a substantial separation (cf. Fig. 3).

We briefly recall the hot-trail effect is visible soon after the beginning of the simulation; at $t \approx 100 P_{orb}$ there are developed oscillations of $r(t)$ (which would correspond to the eccentricity up to 0.035). The zero-torque radius in the absence of accretion heating would be located at about 7 au where the disk becomes flared by stellar irradiation. Instead, we see that planets

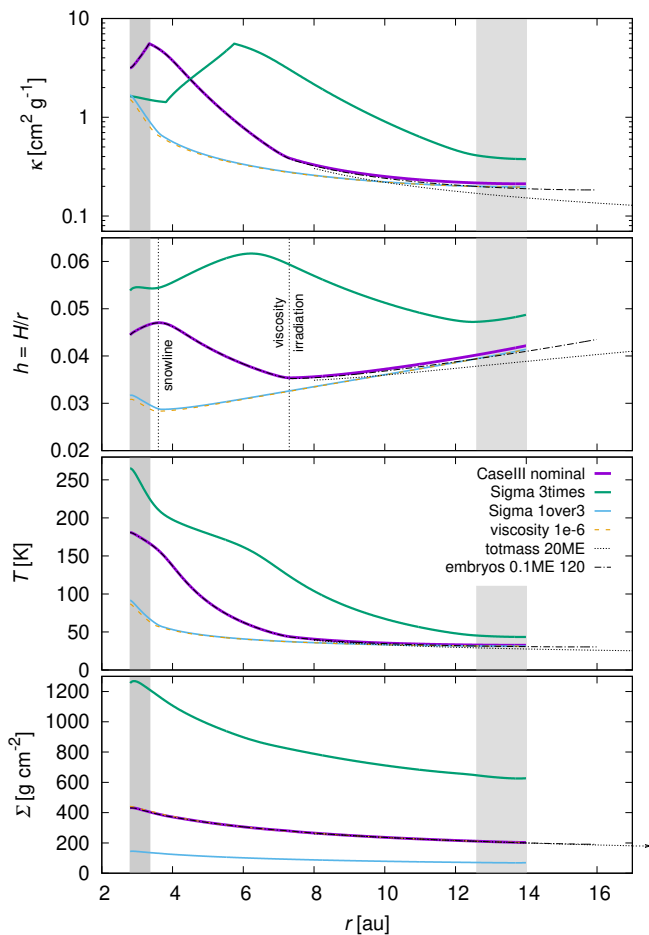


Fig. 1. Profiles of the gas disk after the relaxation phase, which serve as the initial conditions for our simulations. From top to bottom: the opacity κ , the aspect ratio $h = H/r$, the temperature T , and the surface density Σ . The gray boxes indicate the extent of the damping zones at the inner and outer BC. The vertical dotted lines show the snowline, and the transition between the viscous heating and the stellar irradiation regions, in case of the nominal simulation. Some of the simulations actually use the same disk as the nominal one. For `totmass_20ME` simulation we had to use an outer disk, spanning from 8 to 40 au. Similarly, we used a slightly larger disk (up to 16 au) for the simulation `embryos_0.1ME_120`.

migrate towards 9 au. Such an offset is due to the accretion heating, which adds a positive torque contribution, and also the hot-trail effect, because the Lindblad and corotation torques become modified for oscillating orbits.

No low-order mean-motion resonances (MMR) are established during migration, partly because embryos were initially too close, so no captures are expected even if the simulation is run longer. Resonances 3:2, 4:3, 5:4, ... were encountered, but a resonant capture would be difficult anyway, because $e > 0$ (Batygin 2015). During a series of close encounters, there are about 20 exchanges when orbits radially swap, 5 repulsions when the distance between orbits increases, and 2 successful mergers, 13.8 and 4.3 M_{\oplus} , which finally settle to a coorbital configuration (Figure 3).

In the following, we show details of two representative events: the merger and the coorbital formation. As a novelty, we realized that 3-body interactions are needed for successful

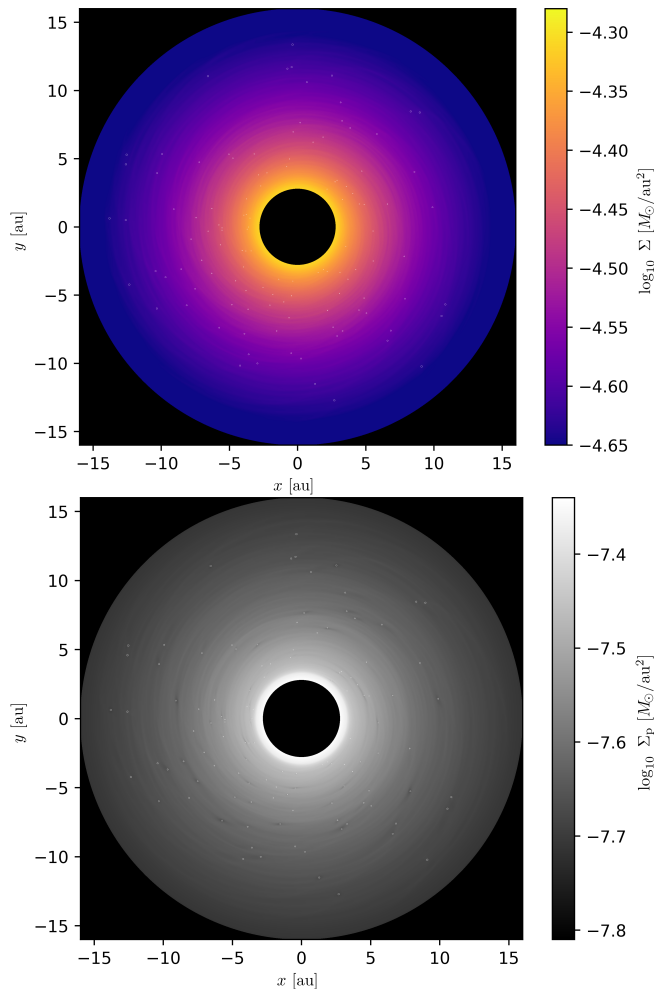


Fig. 2. An initial global structure of the gas and pebble disks in one of our simulations. The gas surface density Σ (top) and the pebble surface density Σ_p (bottom) are shown. In our model the disks interact mutually by means of an aerodynamic drag, and also with protoplanets by means of gravitation (in case of gas) and accretion.

mergers! One can see this already from $r(t)$, that a third embryo is ‘always’ (2 out of 2 cases) present in the vicinity.

3.2.1. Detail: Merger

In order to resolve a detail, the simulation has to be restarted from hydrodynamical field files, prior to the time of interest. We use at least 100 times finer output (every Δt). We have to admit, that the evolution is not always *exactly* the same; for example the SOR method (its relaxation factor) depends on past evolution. Nevertheless, the merger event at $t \doteq 2609 P_{\text{orb}}$ was repeated perfectly, as shown in Figures 4, 5, and B.2.

First, embryo 4 scatters off embryo 3 during a deep encounter, with a minimum separation being a small fraction of the Hill radius, $R_H \doteq 0.15$ au. Second, embryo 4 encounters embryo 2 during the *next* orbit, so they merge. Without the prior strong perturbation, the collision would not occur. At the same time, there are disk torques which substantially affect the evolution (Figure 6). Prior to the merger, they brake the outer embryo 4. It seems that the relative motion in the z -direction is not important in our situation, being a small fraction of the embryo radius, $\Delta z \ll R_{\text{em}} \approx 10^{-4}$ au.

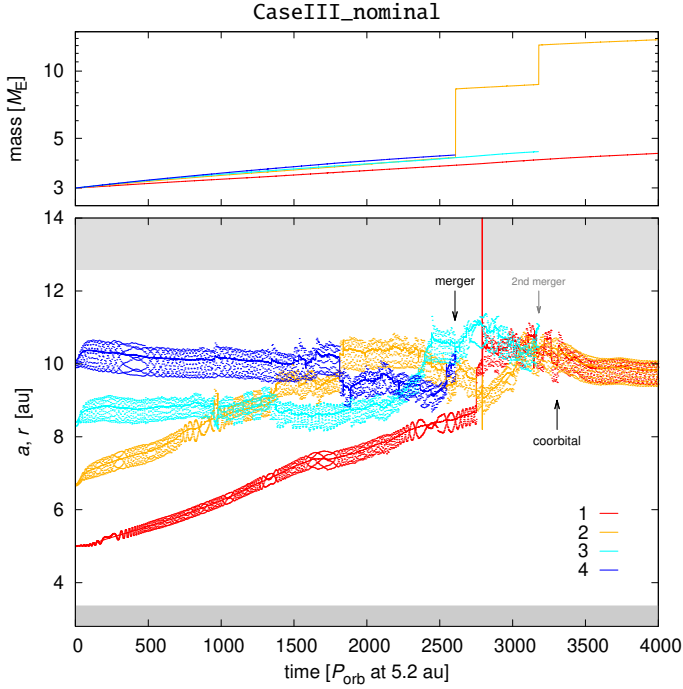


Fig. 3. The semimajor axis a (line), and the heliocentric distance r (dots) vs time t (bottom), and the embryo mass M_{em} vs t (top) for the nominal simulation with initially 4 embryos. The time span $4000 P_{\text{orb}}$ corresponds to 47.4 kyr. Although it was already presented in Chrenko et al. (2017), we show it here to provide an easy (1:1) comparison. The gray strips indicate the inner and outer damping regions used to *gradually* suppress spurious reflections. The black arrows indicate two interesting events we study in detail: a merger (3+4), and a coorbital formation. The semimajor axis may exhibit a ‘spike’ during a close encounter, but in fact $r \ll a$; the body is far from the damping zone.

We also performed a test with a purely N-body integration, in order to check, whether this event is caused either by a mutual gravitational interaction between the embryos, or by hydrodynamics. The integration was restarted from the same time, the derivatives being the same, but without any disk torques, the orbits are Keplerian most of the time, so both encounters have different geometries and a merger event does not occur at all. One can see the actual difference in Fig. 5.

3.2.2. Detail: Coorbital

As shown in Figure 7, the coorbital was formed at $t \doteq 3310 P_{\text{orb}}$ by an encounter of the less-massive embryo 1 with the more-massive embryo 2 from behind. During the approach, embryo 1 flies through a detached, or prolonged spiral arm of embryo 2. The corresponding disk torque suddenly changes from negative to positive (normalized $\Gamma \simeq 50$; Fig. 6). We stress these torques would be calculated wrong in N-body models which use prescriptions derived for single planets. On the departure, the former embryo enters an underdense region and is captured in the coorbital region of the latter.

While we do not model a long-term evolution of the coorbital pair here, we can assume its stabilisation according to Sec. 3.6. Similarly as before, without the disk torques, only an orbital exchange would occur. Coorbitals are generally common outcomes of the simulations, because the resonant captures are prevented by non-zero eccentricities.

3.3. High surface density

For the surface density 3 times larger than the nominal case, as in the *Sigma_3times* simulation, the surface-density structures of the hot trail effect are not so pronounced, owing to the larger thermal capacity of the gas (i.e. specific multiplied by Σ). The temperature excess reaches up to 10 K, not 20 K as before. The 0-torque radius is located further out at approximately 11 au. The oscillations $r(t)$ are relatively small, with the radial distance systematically smaller than the semimajor axis, $r < a$, because the interior disk mass $\int \Sigma(r) 2\pi r dr \simeq 0.03 M_{\odot}$ is no longer negligible. This is also a notable case of non-Keplerian orbits, and a ‘false’ osculating eccentricity $e > 0$, which shall not be used anymore. Generally, the evolution seems slower, although the time span in Figure 8 is almost three times longer and the migration rate is comparable to the nominal case, $da/dt \simeq 10^{-3} \text{ au}/P_{\text{orb}}$.

Embryos do *not* interact so strongly, their orbits stay next to each other for a prolonged period of time, likely because the hydrodynamical eccentricity damping is strong. Sometimes, there is a reverse inward migration of the inner embryo 1 or 2, inducing also larger oscillations of $r(t)$. Moreover, these excursions seem to be often out of phase, and so they are not of a resonant, but rather of a hydrodynamical origin.

Interestingly, there are more than 10 attempts of embryo 3 or 4 to enter the coorbital region of each other. More specifically, there are in total 17 repulsions, 20 exchanges, 2 temporary coorbitals, and eventually 1 merger, again soon after an encounter with another embryo. The last part is already affected by interactions with the disk edge and the damping zone, which kills the outer spiral arm.

3.3.1. Detail: Repulsion

A detail of a repulsion event is shown in Figure 9, namely the first one at $t \doteq 1945 P_{\text{orb}}$. The embryos 3 and 4 approach each other in the apocentre and pericentre, respectively, and their spiral arms are thus aligned. At the minimum distance of just $2R_{\text{Hill}}$, there is an overdensity between them.

The disk torque during this event is shown in Figure 6, in comparison with other types of events. It seems there are alternating torques for the inner and outer embryos, which contribute to the repulsion of the two. The next encounter is consequently more distant. An alternative Figure B.3 expressed in terms of the semimajor axis $a(t)$ also shows the closest encounter itself is driven by the interaction between the embryos, and the disk torque acts as a perturbation. Nevertheless, the regular and repeated nature of these repulsion events confirms that the torque actually determines the encounter geometry.

3.4. Low surface density

Generally, one would expect two limits exist: for $\Sigma \rightarrow \infty$ the thermal capacity is so large, no hot-trail effect can develop; for $\Sigma \rightarrow 0$ there is no hot-trail, because of no gas. In the simulation *Sigma_1over3*, we use the surface density corresponding to 1/3 of the nominal (Figure 10). It turns out the hot trail is even larger compared to the nominal case. This is a result of smaller thermal capacity, and also lower disk temperature which allows for a larger temperature excess. Its development takes longer (more than $200 P_{\text{orb}}$), and the trajectories seem to be more regular.

Overall the migration rate is comparable, although later the motion often exhibits ‘jumps’, because the hydrodynamical damping is weaker. There are: 28 exchanges, 9 repulsions (at least), 0 coorbitals, and 0 mergers in the course of the evolution.

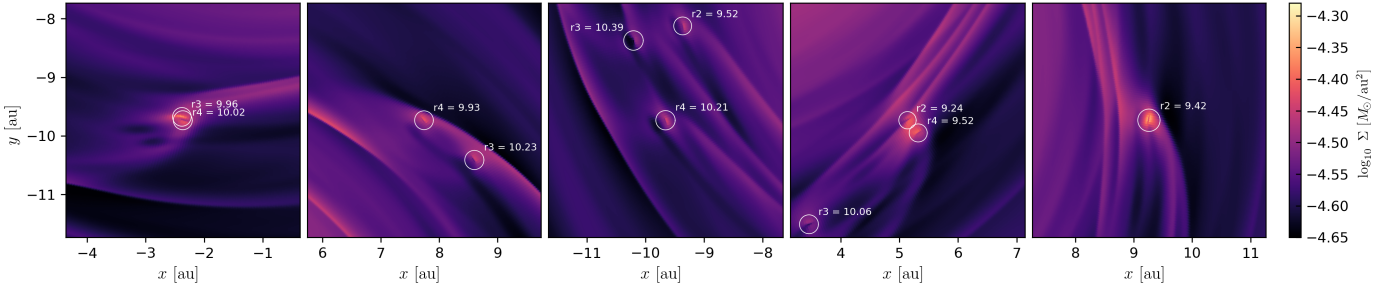


Fig. 4. The gas surface density Σ in the (x, y) plane for a very short segment ($t = 2605$ to $2610 P_{\text{orb}}$ at 5.2 au) of the CaseIII_nominal simulation, showing approximately 1 long-period orbit during which a 3-body interaction occurs, and results in a merger event. The y -coordinates are different for individual panels, but the overall range is always 4 au. The Sun is located at $(0, 0)$. The positions of the embryos are indicated by their Hill spheres (circles), and heliocentric distances (labels, in au units). The motion is in a counter-clockwise sense.

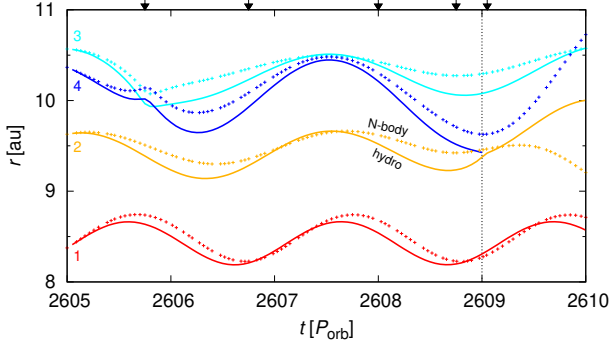


Fig. 5. The heliocentric distance r vs time t for all four embryos in the simulation shown in Fig. 4. The black triangles correspond to the time of individual snapshots. There is an output from the full hydrodynamic simulation (lines), and an N-body simulation with no disks, no torques (points) for comparison. The latter was restarted from the very same initial conditions, at $t = 2605 P_{\text{orb}}$. One can see the merger event at $t \approx 2609 P_{\text{orb}}$. In case of the N-body simulation, the evolution is different, because without the disk torques the trajectories are mostly Keplerian, the encounter between embryos 3 and 4 one orbit prior to the merger (2+4) has a different geometry, so the merger actually does not occur.

Given this statistics, it is compatible to the nominal case (after a normalisation to the same time span $4000 P_{\text{orb}}$); coorbitals and mergers are a matter of small-number statistics, though. One would need a sample of 10^2 simulations to determine which of the simulations would produce more of these relevant outcomes.

3.5. Low pebble flux

Yet another limit is clear: for $\dot{M}_p \rightarrow 0$ the heating is zero and the hot-trail effect too. The opposite case $\dot{M}_p \rightarrow \infty$ is unclear (and unrealistic). For the simulation pebbleflux_2e-5 we choose the pebble flux 10 times lower, corresponding to the embryo growth rate only $0.25 M_{\oplus}$ per $4000 P_{\text{orb}}$. This may be actually more realistic in later phases (Lambrechts & Johansen 2014); the nominal case was on the high side, so we consider this simulation to be potentially very important.

As expected, hot-trail oscillations take longer to develop ($1000 P_{\text{orb}}$), and they are about three times smaller afterwards (Figure 11). The evolution is consequently more smooth, with no 'jumps', until the embryos migrate to the convergence zone at about 11 au. This value seems somewhat surprising, because the heating is substantially lower, and the 0-torque radius should

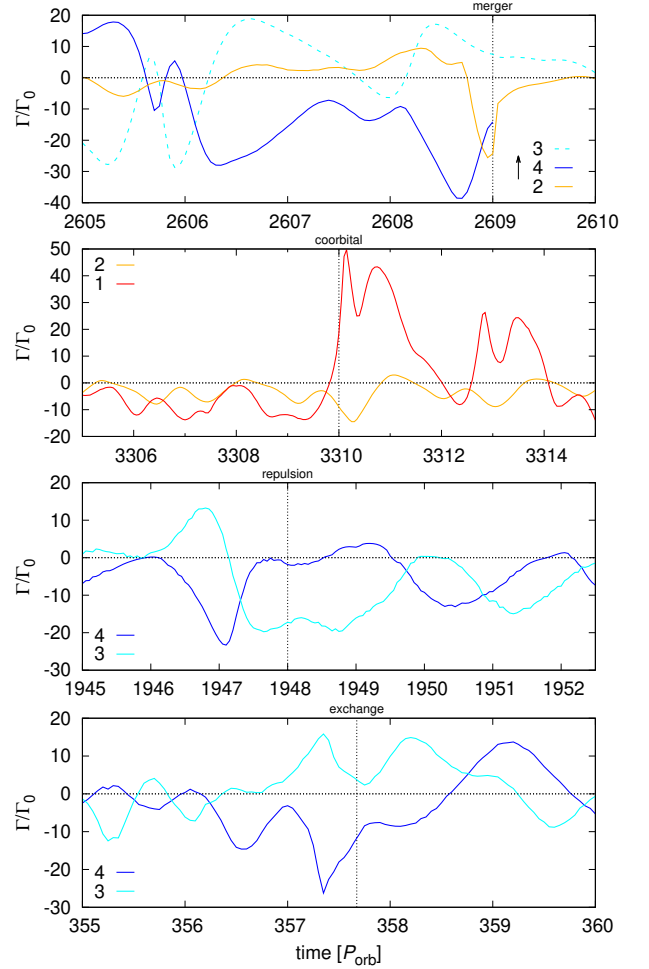


Fig. 6. The normalized total disk torque Γ/Γ_0 vs time t , where $\Gamma_0 = (q/h)^2 \Sigma r^4 \Omega^2$, $q = M_{\text{em}}/M_{\star}$, for four events studied in detail: a merger (top), a coorbital formation, a repulsion, and an exchange (bottom). These events were selected from the following simulations: CaseIII_nominal, ditto, Sigma_3times, viscosity_1e-6. Only those embryos which take part in the interaction are plotted. The label order corresponds to the (initial) radial distance. Each case exhibits a very different progression of the torque. In particular, there is: (i) strong negative torque acting on the outer embryo (for the merger); (ii) positive torque on the inner embryo (coorbital); (iii) alternating torques on both (repulsion); and (iv) negative torque on the outer and positive on the inner (exchange).

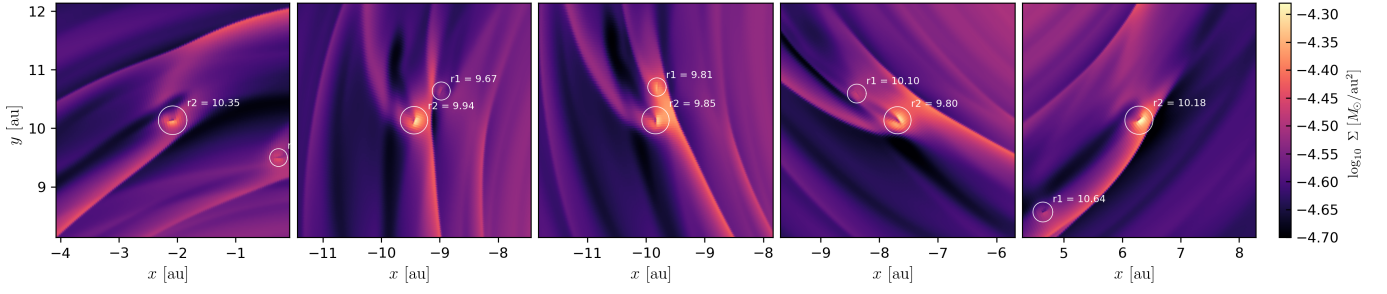


Fig. 7. The same as Fig. 4, but for a coorbital formation during the interval $t = 3305$ to $3315 P_{\text{orb}}$. The less-massive embryo approaches the more-massive from behind, flying through its inner (detached) spiral arm, enters the coorbital region, and flies away in a low density region.

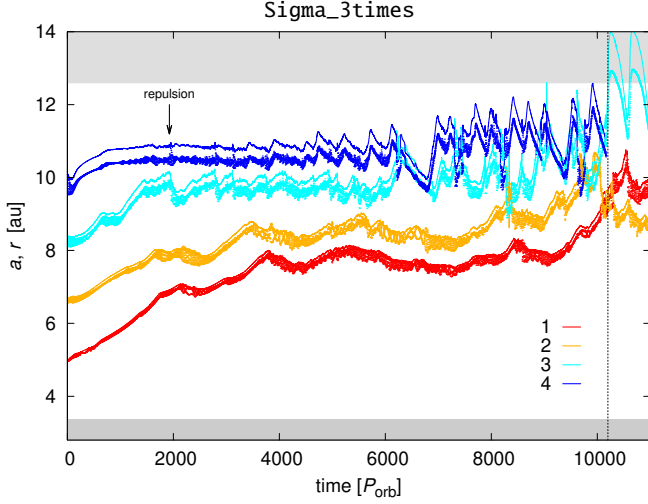


Fig. 8. The semimajor axis a , and the heliocentric distance r vs time t for the simulation Sigma_3times. The convergence radius is shifted further out to 11 au. Merging seems more difficult in this case as there are many ‘repulsions’, especially between embryos 3 and 4. The black arrow indicates the repulsion event we study in detail. Note the semimajor axis is systematically offset from the radial distance, $a > r$, because the orbits are substantially non-Keplerian. After approximately $t \doteq 10000 P_{\text{orb}}$ some unwanted interaction with the disk edge occurs and the evolution is no more reliable. The masses reach 5 to $7 M_{\oplus}$ prior to this.

be rather smaller than the nominal one, $r < 9$ au. However, an equilibrium (of Lindblad, corotation, and heating torques) is perturbed here by the oscillations, and can be therefore shifted elsewhere. For example, a small outward excursion takes the embryo closer to the trailing spiral arm, without actually crossing it, while a large excursion can reverse the Lindblad torque; which is a bit counterintuitive.

The situation later dramatically changes, as there is 1 quick merger, 0 coorbitals, 2 exchanges, 2 big repulsions (plus many small), because the torque acting on the $6 M_{\oplus}$ merger is so strong, it drives it outwards in a runaway mode (Pierens & Raymond 2016). Obviously, this is the explanation for Planet IX. Taken more seriously, it turned out to be a rule for more massive embryos (see Section 3.8). This also leads to a clearing of the outer disk, beyond 11 au. The two remaining embryos 1 and 3 still migrate outwards, their proper 0-torque radius being further out. From the point of statistics, this simulation is not necessarily a representative one, and the early merger can be easily avoided with a minor shift in ICs.

3.6. Low viscosity

As discussed in the Introduction, the disk – or its dead zone with a negligible ionisation and no MRI turbulence – could have been also (almost) inviscid. To this point, we performed a simulation with 10 times lower viscosity (codenamed *viscosity_1e-6*). The structures in the gas disk shown in Figure 12 are more pronounced; the viscous spreading is diminished, thus any density perturbation arising from protoplanets persists longer.

The evolution itself (Figure 13) indicates the same hot-trail oscillations, but a faster migration towards the 0-torque radius (Paardekooper et al. 2011). Embryos pushed by larger torques then interact more violently and this results in: 18 exchanges, 19 repulsions, 2 mergers – created by 3-body interactions – and 5 coorbitals, in total. Out of these, 4 are only temporary, which experience another 3-body interactions, during which exchange their members (around $t \doteq 2000 P_{\text{orb}}$). The last one, formed by two $8 M_{\oplus}$ embryos is stable, and is further stabilized.

This stabilisation is facilitated by a pebble isolation which develops beyond the coorbital pair (Fig. 12, bottom; seen as a stalled accretion $\dot{M}_{\text{em}} \doteq 0$ in Fig. 13, top). It also implicitly drives the migration inwards; it switches off accretion heating by isolating the coorbital from further solid material. The pair is massive enough to create a surface density contrast of about 2 between the interior and exterior part of the gas disk, or 2.5 if we take the middle of the gap. Nevertheless, both are still optically thick; it is not yet a gap opening. Unless there is a substantial filtering of dust (Rosotti et al. 2016), or an extensive shadow hiding the outer part, or very long wavelengths ($\lambda \gg a_{\text{dust}}$) are used, it would be difficult to observe.

3.6.1. Detail: Exchange

A detail of the first exchange is shown in Figure 14. Embryo 3 at the apocentre encounters embryo 4 at the pericentre. An overdense region is formed between them as the outer and inner spiral arms overlap. During the closest approach at a distance of $1.2 R_{\text{H}}$, the gas distribution is uneven. As the embryos become more distant, an extended underdense region is formed between. Disk torques contribute to the exchange, being mostly negative on the outer embryo and positive on the inner one (Fig. 6). Apart from these major perturbations, there are many more minor density waves created by other (inner) embryos.

3.7. Gas accretion

As a test, we performed also a simulation with the gas accretion and the corresponding heating switched on, but the efficiency parameter was very small, $f_{\text{acc}} = 10^{-6}$, as we started with $3 M_{\oplus}$

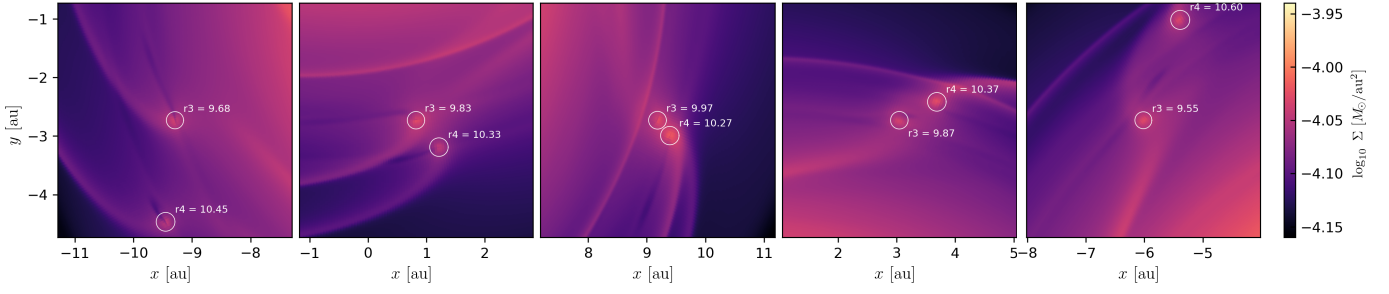


Fig. 9. The same as Fig. 4 for a repulsion event in the Sigma_3times simulation which occurred between $t = 1945$ to $1952 P_{\text{orb}}$. The embryos approach each other in the apocentre and the pericentre respectively, with spiral arms ‘aligned’. There is an overdensity between the Hill spheres during the closest approach, and yet another spiral arm originating from the inner embryo 2 after the close approach.

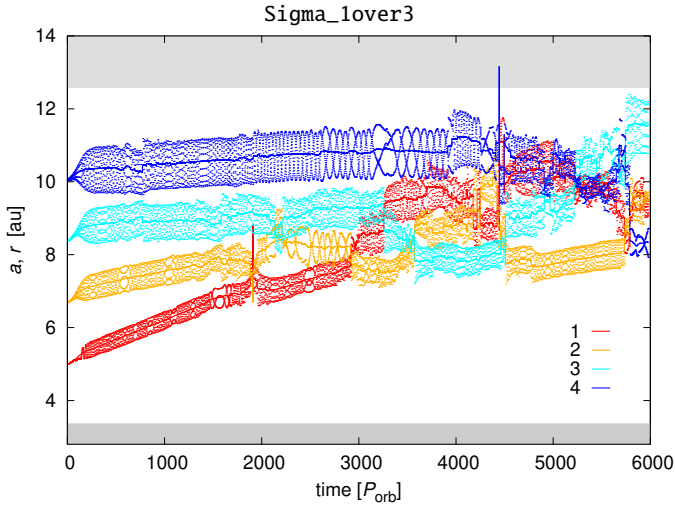


Fig. 10. The same as Fig. 3 for the simulation with Σ_0 three times smaller than the nominal one. The oscillations $r(t)$ induced by the hot-trail effect are larger compared to the previous case, and also seem more stable. There are numerous encounters in the evolution, but no mergers yet. The final masses reach 5 to $6 M_{\oplus}$.

bodies. Specifically, the gas accretion rate is given by the integral over the exponential density profile (Kley 1999):

$$\left(\frac{\partial \Sigma}{\partial t}\right)_{\text{acc}} = \sum_i \frac{1}{3} f_{\text{acc}} \iint \mathcal{H}(|\mathbf{r}_{\perp i} - \mathbf{r}_{\text{cell}}| - 0.75 R_{\text{Hi}}) \times \frac{\Sigma}{\sqrt{2\pi}H} \int_{z_i - \Delta z}^{z_i + \Delta z} \exp\left[-\left(\frac{z}{\sqrt{2}H}\right)^2\right] dz d\theta dr, \quad (10)$$

plus the same term with numerical factors $\frac{2}{3}$ and 0.45, where \mathcal{H} denotes the Heaviside step function, \mathbf{r}_{\perp} the planet position in (x, y) plane, $\Delta z = \sqrt{(0.75 R_{\text{Hi}})^2 - |\mathbf{r}_{\perp} - \mathbf{r}_{\text{cell}}|^2}$, and H the vertical scale height.

The total amount of gas thus reaches at most $0.035 M_{\odot}$. We may regard this simulation more as another realisation of the nominal one. Indeed, according to Figure 15, the hot-trail oscillations are practically the same, and the migration rates too. The difference stems from the chaotic nature of the system. A comparison of the first $4000 P_{\text{orb}}$ shows a similar frequency of the common events, albeit there are no coorbitals or mergers yet, which are simply not frequent enough to occur in every simulation. We did not continue the simulation because of the interactions with the outer damping zone.

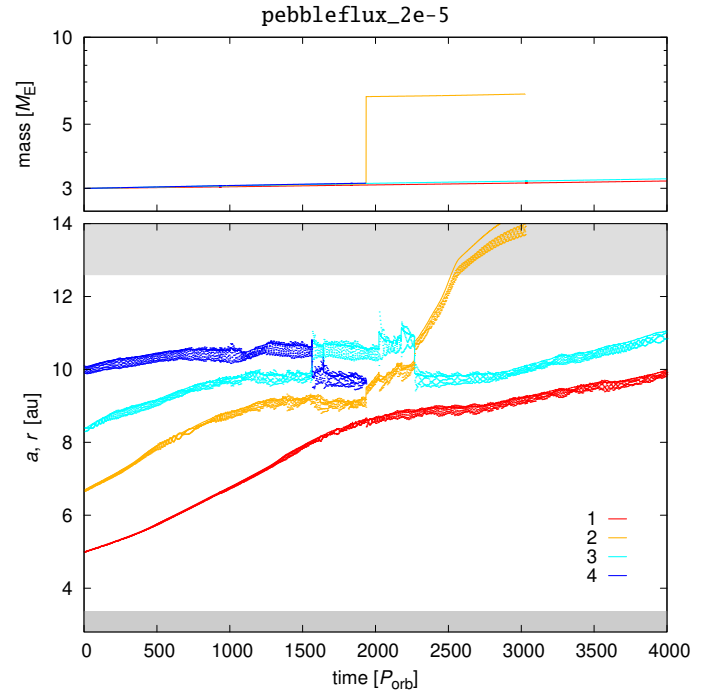


Fig. 11. The same as Fig. 3 for the pebble flux \dot{M}_p ten times smaller than the nominal case. The hot-trail effect (e 's) are then smaller than in the nominal case. After a merger at $t \doteq 2250 P_{\text{orb}}$, the resulting $6 M_{\oplus}$ embryo quickly migrates outwards and is lost at the outer BC.

3.8. Four $5 M_{\oplus}$ embryos

With initial masses $5 M_{\oplus}$ all embryos quickly drifted outwards. The 0-torque is clearly much more distant, and our setup requires an outer disk spanning from 8 to 40 au (i.e. totmass_20ME). In other words, this may be relevant for the formation of ice giants. The spacing of embryos is 16 mutual Hill radii, similarly as before. We also deliberately decreased the pebble flux to $\dot{M}_p = 10^{-5} M_{\oplus} \text{ yr}^{-1}$, because larger embryo masses are usually attained later. A convergence to the new 0-torque radius at about 20 au is relatively fast, especially when longer orbital periods are taken into account (Figure 16).

The evolution is similarly complex as in the inner disk, with 20 exchanges, 5 repulsions (not counting the small ones), 2 mergers, and 2 coorbitals, with the last one (at $t \doteq 4000 P_{\text{orb}}$) stabilised; this time it is not due to the pebble isolation, but rather pebble filtering due to embryo 1, presently the outer massive merger.

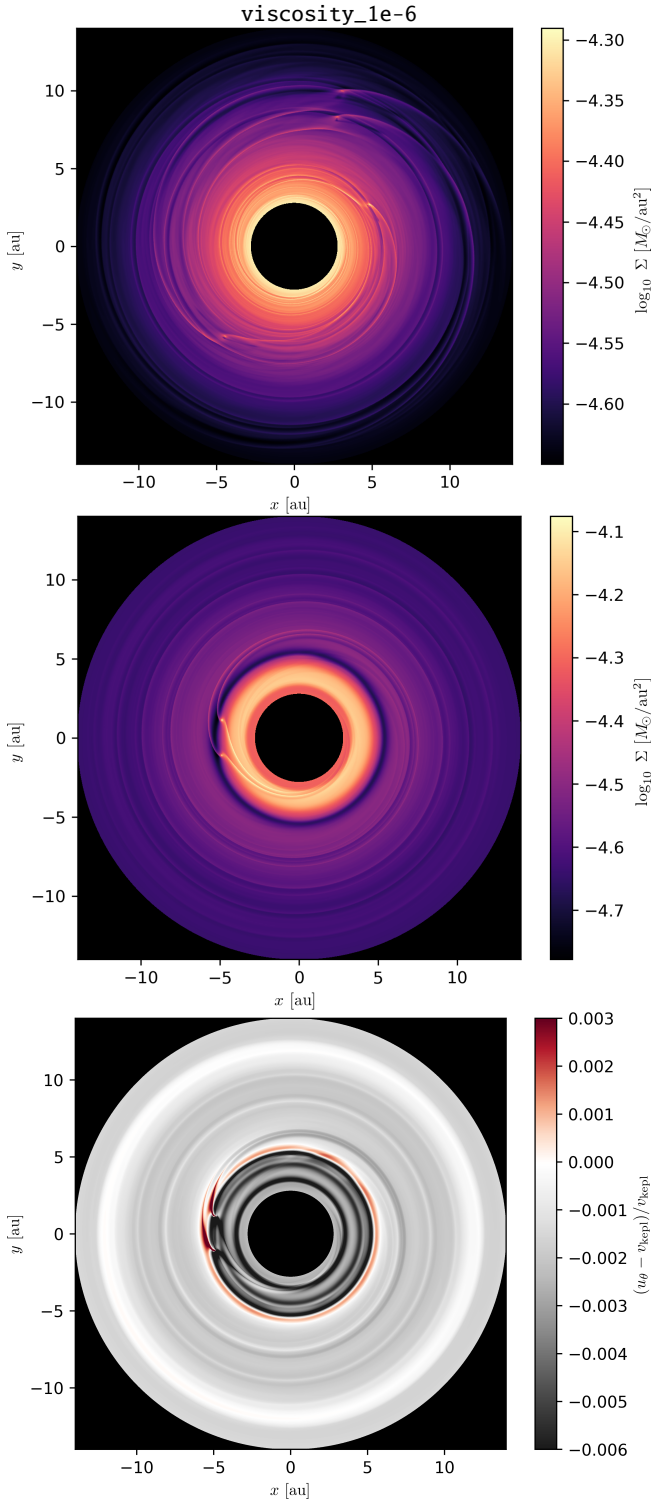


Fig. 12. The surface density Σ for the simulation with ten times smaller viscosity ν ; the situation short after the beginning at $t = 100 P_{\text{orb}}$ (top), and the final state at $t = 8000 P_{\text{orb}}$ (middle). The structures are initially more pronounced compared to the nominal case, because perturbations of the low-viscosity gas spread more slowly. The outcome is a massive coorbital which migrates towards the inner boundary. The density contrast between Σ interior and exterior to the coorbital is about 2; the disk is optically thick in both cases. The corresponding azimuthal velocity $(u_\theta - v_{\text{kepl}})/v_{\text{kepl}}$ of pebbles (bottom), compared to the Keplerian velocity. Just outside the coorbital pair u_θ is positive (super-Keplerian) and a pebble isolation develops.

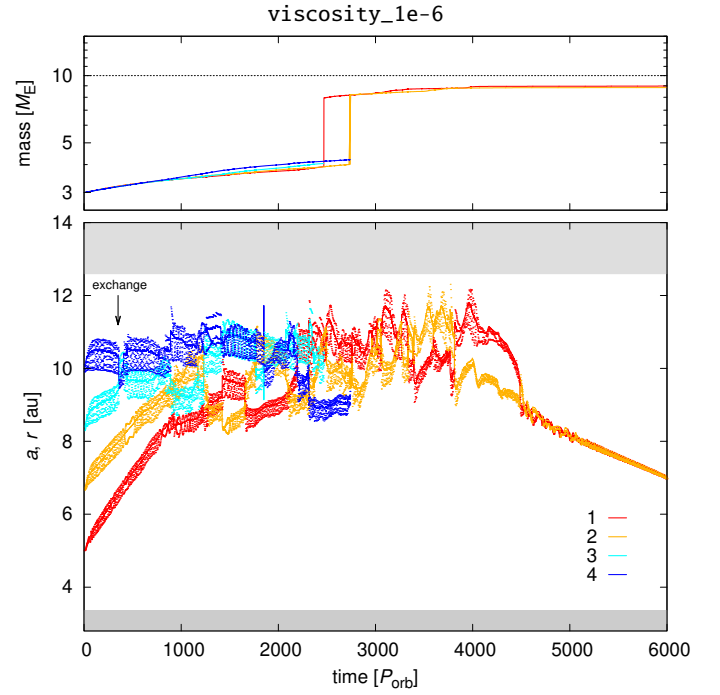


Fig. 13. The same as Fig. 3 for the simulation with ten times smaller viscosity ν . The oscillations $r(t)$ are initially similar to the nominal case, but there is a faster migration towards the convergence radius. After many 'trials', there are two mergers ($8 M_\oplus$), which later form the coorbital pair. The black arrow indicates the repulsion event we study in detail.

A very interesting behaviour then starts: embryo 1 is pushed outwards by a dynamical torque created by an underdense tadpole-like region (Pierens 2015). Later at $t \approx 4900 P_{\text{orb}}$, when embryo 1 reaches its new convergence radius r_c , it slightly overshoots, is pushed backwards and the tadpole region is refilled by a material originating from the inner spiral arm. With no underdensity anymore, embryo 1 is pushed inwards, until it encounters the coorbital. This behaviour is systematically repeated four times, with a disruption of the coorbital in the meantime, and a second merger after all.

3.9. Eight $1.5 M_\oplus$ embryos

For eight embryos with $1.5 M_\oplus$ each, we can see a clear convergence to the 0-torque radius at approximately 9 au (as in the nominal case). The oscillations due to the hot-trail are apparently small for the innermost embryos, but they become larger as they migrate outwards. At the given radial distance, the amplitudes are the same, of course (Figure 17).

The migration is slower compared to the nominal case, nevertheless, the initial spacing is more compact (10 mutual Hill radii), and interactions start at about the same time. They are of all kinds, both two-body and three-body, but we will not count them explicitly, as the number of objects is twice larger. Generally, there are more opportunities to merge, ending up in 5 mergers, the most massive having up to $25 M_\oplus$. From this standpoint, the simulation can be termed as successful, creating a giant-planet core with more than a critical mass. Our current model is not reliable for this large mass though, as we used no Hill cut, zero gas accretion efficiency factor f_{acc} , and there are problems to describe the pebble isolation in 2D (Bitsch et al. 2018). A sixth merger occurred after a series of unwanted in-

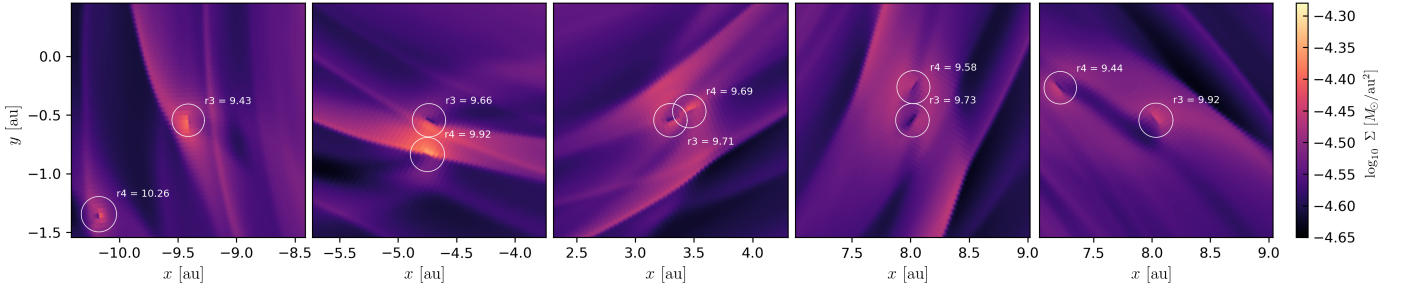


Fig. 14. The same as Fig. 4 for an exchange event in the `viscosity_1e-6` simulation. The embryos 3 and 4 approach in such a way, the inner flies behind the outer, and a shared underdense region is formed which connects the embryos during their retreat.

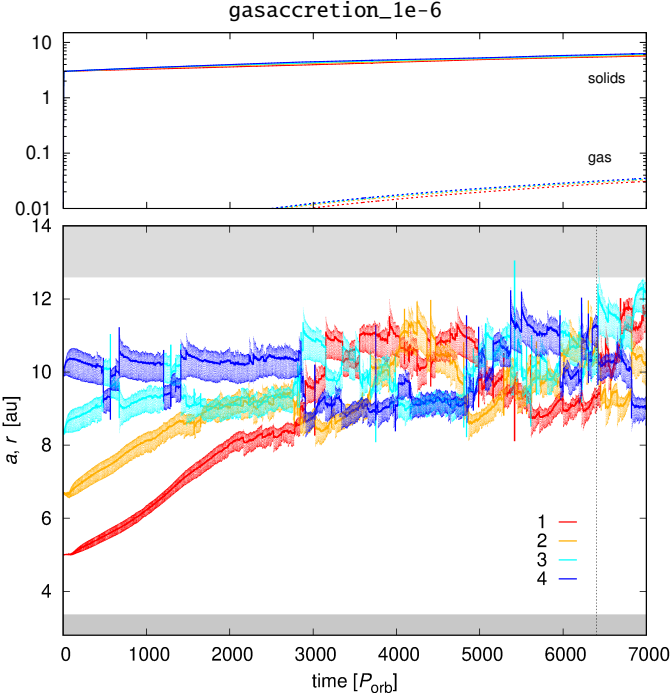


Fig. 15. The semimajor axis a (line), and the heliocentric distance r (dots) vs time t (bottom), and the embryo mass M_{em} vs t (top) for the simulation including the gas accretion, with the efficiency factor $f_{\text{acc}} = 10^{-6}$. We distinguish the solid (solid) and gaseous (dashed) component of M_{em} . Note we used a finer sampling of the orbital elements. Both the migration rates and the eccentricities seem the same as in the nominal case, because the gas accretion contributes only very little to the mass and heating. However, no merging occurred in the course of this simulation. After $t \doteq 6400 P_{\text{orb}}$ there is an interaction with the disk edge and the evolution is no more reliable.

interactions with the outer damping zone, and this makes further evolution also unreliable.

In this simulation (and also in `viscosity_1e-6`), the embryos gain non-negligible temporary inclinations of the order of 10^{-4} rad, despite of Tanaka & Ward (2004) damping. The vertical distances are then orders of magnitude larger than protoplanet diameters, which decreases collisional probabilities. On the other hand, a gravitational focussing (with $v_{\text{esc}} \doteq 7 \text{ km s}^{-1}$) – which is accounted in our model – helps to counteract it.

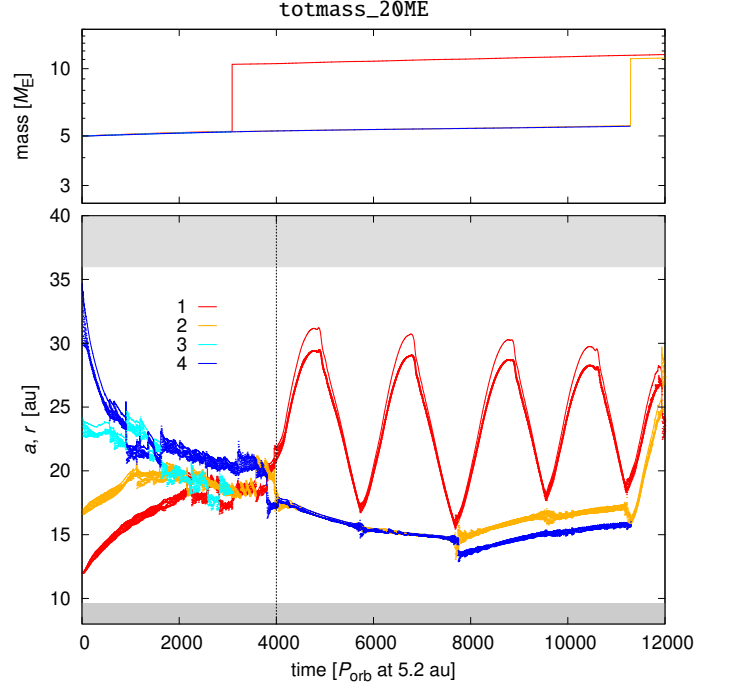


Fig. 16. The same as Fig. 3 for the simulation with $5M_{\oplus}$ embryos. We model an outer disk here, because the convergence radius turned out to be far (21 au). After numerous exchanges, temporary coorbitals, and one merger, a relatively stable coorbital is formed at $t \doteq 4000 P_{\text{orb}}$. Embryo 1 is then pushed outwards by a dynamical torque created by an underdense tadpole-like region (Pierens 2015). At $t \doteq 4900 P_{\text{orb}}$ the tadpole region is refilled by a material originating from the inner spiral arm, and embryo 1 is pushed inwards, until it encounters the coorbital. This behaviour is systematically repeated, and results in a disruption of the coorbital, and a merger.

3.10. Many low-mass embryos

Finally, we simulated a system composed of 120 embryos with $0.1 M_{\oplus}$ each (i.e. `embryos_0.1ME_120`); the total mass remains the same as the nominal. We chose a tight spacing of 2 mutual Hill radii:

$$R_{\text{HH}} = \frac{1}{2}(a + a') \left(\frac{q + q'}{3} \right)^{1/3}, \quad (11)$$

with a the semimajor axis and q the planet-to-star mass ratio, to fit all bodies in a disk spanning from 2.8 to 16 au. The initial state was already shown in Figure 2. A convergence test for a single embryo is presented in Appendix A. Our current resolution is still low, 3 cells per Hill sphere. The test shows that

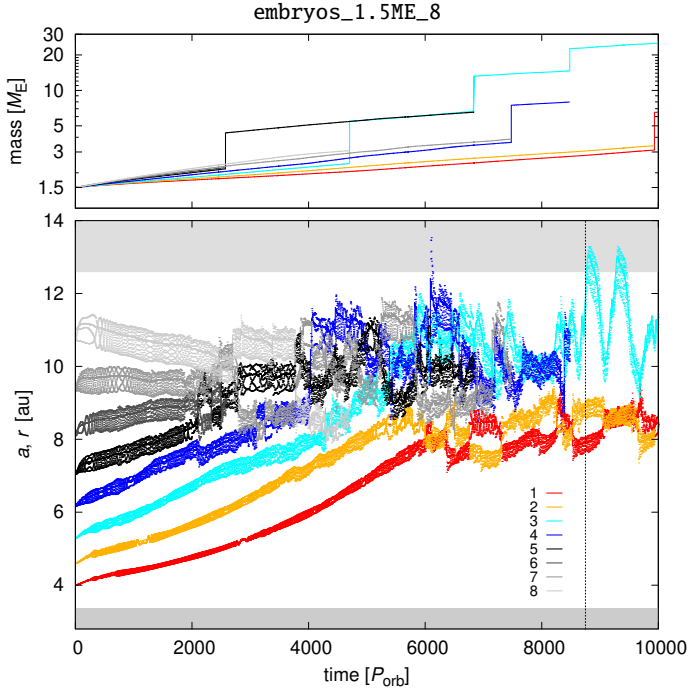


Fig. 17. The same as Fig. 3 for the simulation with eight $1.5M_{\oplus}$ embryos. The evolution seems qualitatively similar to the nominal case, with 6 merger events amidst. Most if not all mergers occur when 3-body interactions take place. After $t \doteq 8750 P_{\text{orb}}$ an interaction of the outer embryo with the disk edge occurs and the evolution is no more reliable.

da/dt is then overestimated by a factor of 3, and $r(t)$ oscillations (or eccentricity e) have the same amplitude. We consider this as an acceptable approximation which may somewhat enhance the efficiency of merging (due to larger da/dt). Having correct eccentricities seems more important to prevent spurious resonant captures. It is a very slow computation anyway, with 120 disk \leftrightarrow planet interactions; to this point it was run on the NASA Pleiades supercomputer, with 10^3 reserved CPU cores, and a combined MPI/OpenMP parallelisation. To better resolve the Hill sphere, one would have to increase the number of cells in *both* radial and tangential directions, fulfill the Courant condition in these smaller cells, and compute all the interactions, so it scales almost as $N^3 N_{\text{em}}$.

The most important result is visible already at the beginning – there is no smooth Type-I migration, because there are no regular patterns (see Figure 18)! The weak spiral arms overlap, and affect neighbouring corotation regions too. These *stochastic torques* are very different from the classical, regular, single-planet torques. Although Type-I migration in its simplest form may be considered linear, it is no longer true, because our system of equations (Eqs. (1) to (7)) includes several non-linear terms (T^3 , T^4 , Q_{visc}). Mutual gravitational interactions of the embryos also partly contribute to the stochastic nature of the system, especially given the initial spacing ($2R_{\text{HH}}$).

The evolution of the whole system is surprisingly slow (Figure 19). The oscillations induced by the hot-trail effect ($e \doteq 0.02$) serve as an initial ‘kick’, which leads to numerous close encounters. At the same time, inclinations i are excited too, being virialised with the eccentricities e . The average values are different though, $e \simeq 0.02$, $i \simeq 0.01$ rad, because Tanaka & Ward (2004) damping acts on inclinations. This is a new situation; in all previous simulations inclinations remained low (less

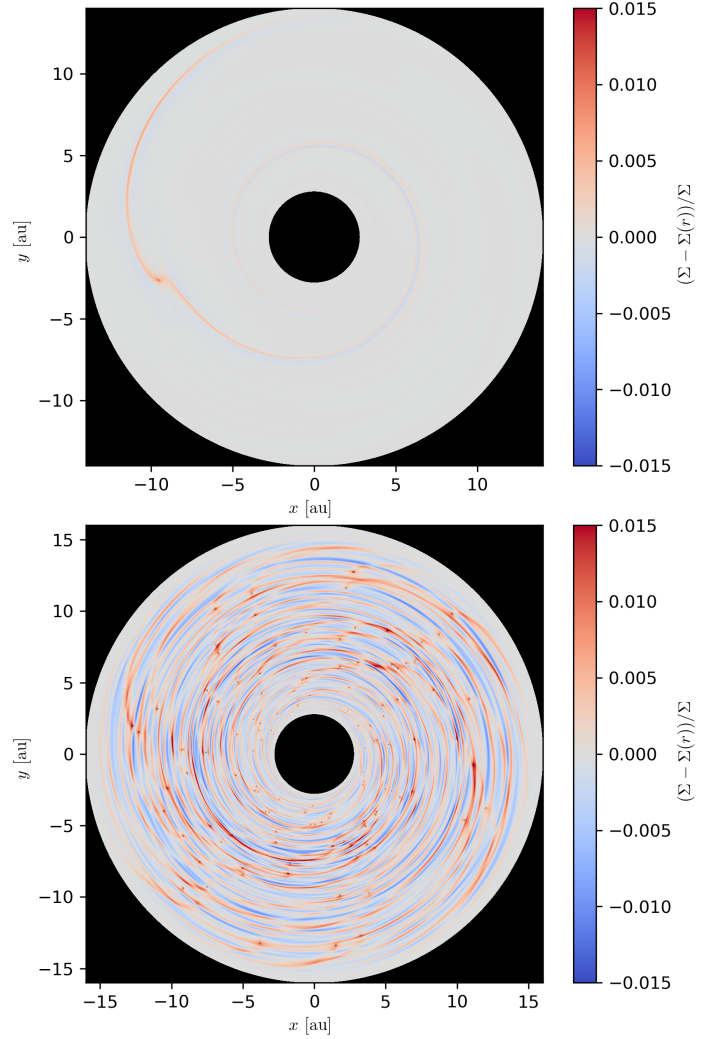


Fig. 18. The surface density $\Sigma(r, \theta)$ of the gas disk with the azimuthally averaged profile $\Sigma(r)$ subtracted to clearly see the respective spiral arms, the corotation region, and other perturbations the surroundings of the Hill sphere. The system was evolved for 100 orbital periods P_{orb} (at 5.2 au) so that the hot trail effect can develop and increase the eccentricity. The situation is very different for a single $0.1 M_{\oplus}$ embryo (top), with a very regular spiral, and for 120 embryos with the same masses (bottom), with spiral arms overlapping each other, and creating an irregular overall pattern. The situation corresponds to Fig. 2, but it is much easier to see the perturbations when $\Sigma - \Sigma(r)$ quantity is used. The resolution 3072×4096 was used for the former short-term simulation, and 2048×3072 for the latter. The Hill spheres are shown as small black circles.

than 10^{-3} even during close encounters). Given the increase of e , we expected there will be many mergers early in the simulation, but this is suppressed by the increase of i . There are only 11 of them which occur during the first few $100 P_{\text{orb}}$, creating a group of $0.2M_E$ embryos, located both in the inner and outer parts of the disk. It might be an artifact of our initial conditions, but it does not ‘hurt’ us in any way, because having some range of masses initially seems even more realistic.

Further growth is facilitated mostly by the pebble accretion. Only a handful of additional mergers occur (see Fig. 19, top). We identified five processes which contribute to a runaway growth: (i) the initial mergers ($0.2 M_{\oplus}$), other embryos have a mass

‘handicap’; (ii) in the Hill regime of pebble accretion the cross section is proportional to the embryo mass, $\pi R_H^2 \propto M_{\text{em}}^{2/3}$, and the relative velocity too, $v_H \propto R_H \propto M_{\text{em}}^{1/3}$, which results in an exponential $M_{\text{em}}(t)$ evolution; (iii) late mergers of inner embryos occur, which subsequently drift outwards; (iv) pebble filtering by outer (already massive) embryos; (v) a separation between low- and high-mass embryos, with the former having larger *mean* inclinations than their pebble feeding zone (Figure 20). The peak masses are almost $3 M_{\oplus}$ for the group of early mergers, while only $0.6 M_{\oplus}$ for the group of original embryos.

The pebble filtering is closely related to a ‘gap’ which develops in the pebble disk (Figure 21, bottom). Pebbles drifting inwards experience a strong filtering, Σ_p decreases as $r \rightarrow 0$. The apparent increase of Σ_p at $r \simeq 6$ au is only due to a flux conservation towards the centre. The ‘winner’ embryo is consequently located in the outer part of the disk, because it experiences almost no filtering.

The separation of inclinations, or in other words a viscously stirred pebble accretion, was studied by Levison et al. (2015), using a Lagrangian approach. Indeed, in our case $\tau \simeq 0.05$, $\alpha_p = 10^{-4}$, $H_p/H = \sqrt{\alpha_p/\tau} \simeq 0.045$, $h = H/r \simeq 0.04$, $h_p = \tan I_p \simeq 0.0018$, i.e. a similar value as in their work.

Finally, the most massive embryos exhibit a systematic drift towards a 0-torque radius at approximately 11 au, although it is somewhat hidden in Fig. 19. Low-mass ones randomly walk (with a \sqrt{t} characteristic). As soon as they reach the interaction zone of high-mass ones, they start to randomly ‘run’, because the zone is very chaotic.

Luckily, the final state of the system is quite similar to the initial conditions of the simulation CaseIII_nominal. There are 4 embryos with masses between 1.5 and $3 M_{\oplus}$. They are already located close to the 0-torque radius and they already interact with each other. We do not think this is a mere coincidence, but rather an indication our model can self-consistently describe both phases of evolution in one ‘elegant’ step.

4. Conclusions

The simulations of the Type-I migration presented in this study confirm that outcomes sensitively depend on the disk parameters, as well as the initial conditions and masses of protoplanets. We reported at least several interesting results: (i) three-body encounters are needed for successful mergers; (ii) in high- Σ disks (several times MMSN) ‘repulsion’ events are frequent; (iii) a massive coorbital pair may develop a pebble isolation which prevents further accretion; (iv) a stabilisation and inward migration of the coorbital then occurs; (v) a dynamical tadpole torque can arise in the outer disk (as in Pierens 2015); (vi) this leads to outward \leftrightarrow inward migration cycles; (vii) the respective fast-migrating embryo may disrupt an inner coorbital pair, solving the problem of too many coorbitals which are not observed (Vokrouhlický & Nesvorný 2014); (viii) disk torques for many low-mass embryos are stochastic, due to overlapping spiral arms, and the torques computed for single planets (as in Paardekooper et al. 2011) are no longer valid in this regime. This may have very important implications for N-body models of planetary migration.

In the gas-giant zone, our simulations show a robust runaway growth with several contributing processes, in particular the above mentioned merging of embryos, the Hill regime of pebble accretion which is proportional to M_{em} , the pebble filtering by outer embryos, and lower inclinations of massive em-

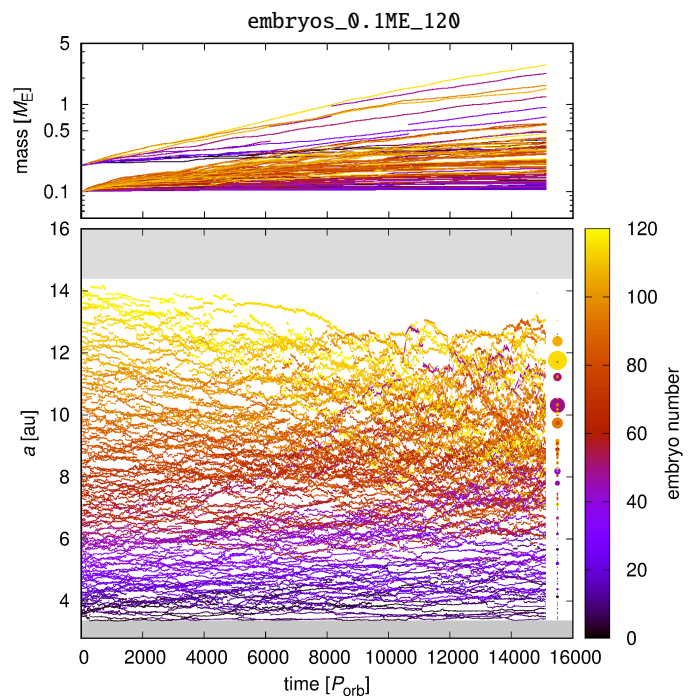


Fig. 19. The semimajor axis a vs time t (bottom), and the embryo mass M_{em} vs t (top) for the simulation with 120 low-mass $0.1 M_{\oplus}$ embryos. Colours correspond to the embryo number to distinguish the individual orbits. The final state is depicted as a series of filled circles, with sizes proportional to the masses. The evolution is never regular but rather chaotic, partly due to direct N-body gravitational interactions among the embryos, but more importantly due to overlapping spiral arms (see also Fig. 18). Initially, there are only several mergers which create a handful of $0.2 M_{\oplus}$ embryos. These grow preferentially by the pebble accretion; there are a few additional mergers.

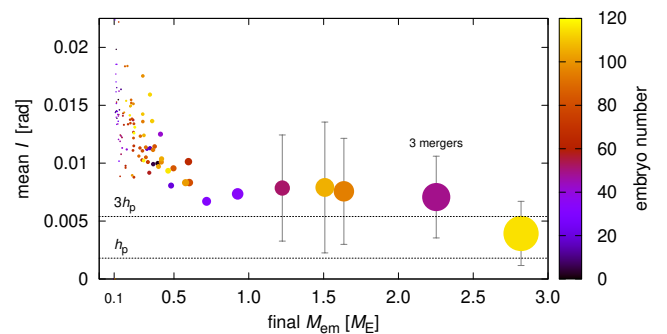


Fig. 20. The mean inclination \bar{I} (radians) versus the final embryo mass M_{em} . The symbol sizes correspond also to M_{em} and their colours to the embryo number, or its initial position. The horizontal dotted lines indicate multiples of the pebble scale height, $h_p = H_p/r$. The smaller vertical distance of the massive embryos from the pebble disk contributes to a runaway growth. All embryos are already in the Hill regime, and their effective accretion radius ranges from $R_{\text{eff}}/r = 0.003$ to 0.012 .

bryos (being often within the pebble disk scale height), further supporting the results of Levison et al. (2015).

In the ice-giant zone (at 20 au), there is a surprising convergence zone for more massive ($5 M_{\oplus}$) embryos, or mergers which may originate from the gas-giant zone. This could possibly sup-

port scenarios in which Neptune forms first, Uranus second, etc. – in an opposite way than in Izidoro et al. (2015).

We may be actually seeing different phases of a ‘Grand Scenario’, outlined e.g. by the following sequence of simulations: `embryos_0.1ME_120` → `embryos_1.5ME_8` → `pebbleflux_2e-5` → `totmass_20ME`. Of course, it would be better to have everything in one simulation (and a big disk, spanning at least from the water snowline to the outer edge, if there was any).

The time span of our longest simulations is about 150 kyr. If the total available mass of solids is of the order of $130 M_{\oplus}$ (as in Levison et al. 2015), and the pebble flux reaches up to $2 \times 10^{-4} M_{\oplus} \text{ yr}^{-1}$, its duration could be as long as 650 kyr. It is thus still possible to prolong our simulations using the current setup.

Ideally, one would like to continue until the gap opening in the gas disk, which would however require a better treatment of the pebble isolation (Bitsch et al. 2018); a suitable parametrisation of the gas accretion, derived in full 3D, not in 2D (Crida & Bitsch 2017); or even until the photoevaporation, probably including a model for the disk atmosphere (Owen et al. 2011), and inevitably also a planetesimal (debris) disk, which stabilises the emerging compact planetary systems.

Acknowledgements

The work of MB and OC has been supported by the Grant Agency of the Czech Republic (grant no. 13-06083S). The work of OC has been supported by Charles University (research program no. UNCE/SCI/023; project GA UK no. 128216; project SVV-260441). DN’s work was supported by the NASA XPR program. Access to computing and storage facilities owned by parties and projects contributing to the National Grid Infrastructure MetaCentrum, provided under the programme ‘‘Projects of Large Research, Development, and Innovations Infrastructures’’ (CESNET LM2015042), is greatly appreciated. We also thank A. Morbidelli and E. Lega for fruitful discussions on the subject, an anonymous referee and the editor (T. Guillot) for constructive criticism.

References

- Anderson, J. M., Li, Z.-Y., Krasnopolsky, R., & Blandford, R. D. 2005, *ApJ*, 630, 945
- Bae, J., Nelson, R. P., & Hartmann, L. 2016, *ApJ*, 833, 126
- Balbus, S. A. & Hawley, J. F. 1991, *ApJ*, 376, 214
- Batygin, K. 2015, *MNRAS*, 451, 2589
- Bell, K. R. & Lin, D. N. C. 1994, *ApJ*, 427, 987
- Benítez-Llambay, P., Masset, F., Koenigsberger, G., & Szulágyi, J. 2015, *Nature*, 520, 63
- Benítez-Llambay, P. & Pessah, M. E. 2018, *ApJ*, 855, L28
- Bitsch, B., Crida, A., Morbidelli, A., Kley, W., & Dobbs-Dixon, I. 2013, *A&A*, 549, A124
- Bitsch, B., Morbidelli, A., Johansen, A., et al. 2018, *A&A*, 612, A30
- Bitsch, B., Morbidelli, A., Lega, E., Kretke, K., & Crida, A. 2014, *A&A*, 570, A75
- Chiang, E. I. & Goldreich, P. 1997, *ApJ*, 490, 368
- Chrenko, O., Brož, M., & Lambrechts, M. 2017, *A&A*, 606, A114
- Coleman, G. A. L. & Nelson, R. P. 2016, *MNRAS*, 457, 2480
- Crida, A. & Bitsch, B. 2017, *Icarus*, 285, 145
- Crida, A. & Morbidelli, A. 2007, *MNRAS*, 377, 1324
- Eklund, H. & Masset, F. S. 2017, *MNRAS*, 469, 206
- Espaillet, C., Muzerolle, J., Najita, J., et al. 2014, *Protostars and Planets VI*, 497
- Günther, H. M. 2013, *Astronomische Nachrichten*, 334, 67
- Hubeny, I. 1990, *ApJ*, 351, 632
- Ida, S., Guillot, T., & Morbidelli, A. 2016, *A&A*, 591, A72
- Ingleby, L., Calvet, N., Herczeg, G., et al. 2013, *ApJ*, 767, 112
- Izidoro, A., Morbidelli, A., Raymond, S. N., Hersant, F., & Pierens, A. 2015, *A&A*, 582, A99

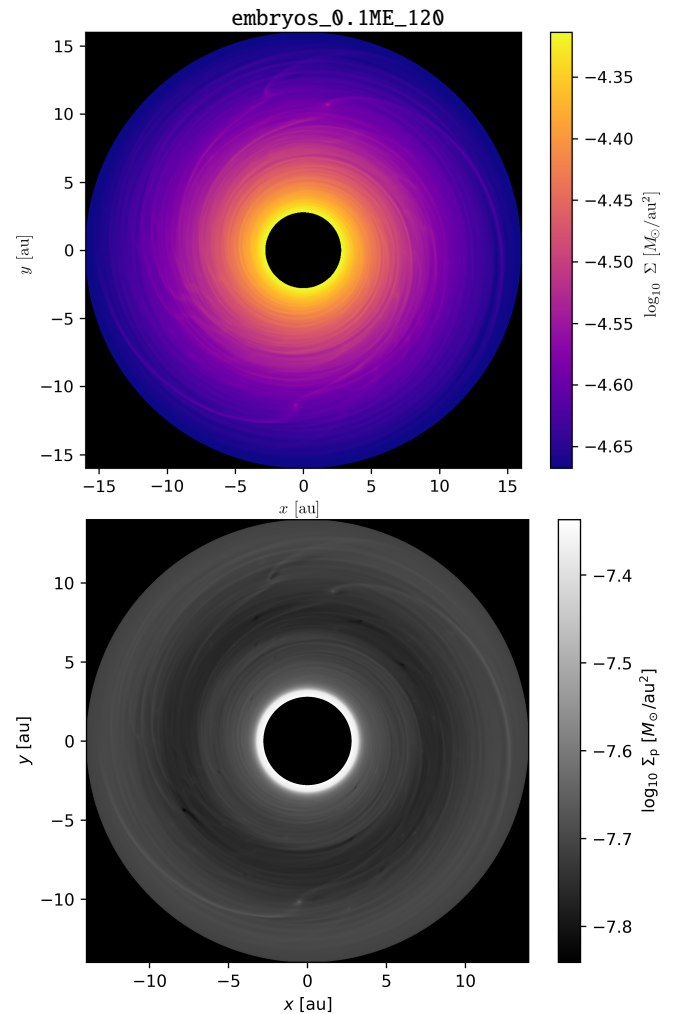


Fig. 21. The gas surface density Σ (top) and the pebble surface density Σ_p close to the end of the simulation `embryos_0.1ME_120`, at $t = 11200 P_{\text{orb}}$. It is a continuation from Fig. 2. There are relatively massive embryos present in the disk, reaching up to $3 M_{\oplus}$ (cf. the spiral arms). They concentrate in the outer part of the disk. In the pebble disk, one can see a darker region (low Σ_p) in the middle which arises from a substantial pebble filtering by the outer embryos. The resolution 1024×1536 was used for this long-term simulation.

- Izidoro, A., Ogiyara, M., Raymond, S. N., et al. 2017, *MNRAS*, 470, 1750
- Klahr, H. & Kley, W. 2006, *A&A*, 445, 747
- Klahr, H. H. & Bodenheimer, P. 2003, *ApJ*, 582, 869
- Kley, W. 1989, *A&A*, 208, 98
- Kley, W. 1999, *MNRAS*, 303, 696
- Kley, W. & Dirksen, G. 2006, *A&A*, 447, 369
- Lambrechts, M. & Johansen, A. 2012, *A&A*, 544, A32
- Lambrechts, M. & Johansen, A. 2014, *A&A*, 572, A107
- Lambrechts, M. & Lega, E. 2017, *A&A*, 606, A146
- Levison, H. F., Kretke, K. A., & Duncan, M. J. 2015, *Nature*, 524, 322
- Lin, D. N. C. & Papaloizou, J. 1986, *ApJ*, 307, 395
- Masset, F. 2000, *A&AS*, 141, 165
- Mihalas, D. & Weibel Mihalas, B. 1984, *Foundations of radiation hydrodynamics*
- Müller, T. W. A., Kley, W., & Meru, F. 2012, *A&A*, 541, A123
- Nelson, R. P., Gressel, O., & Umurhan, O. M. 2013, *MNRAS*, 435, 2610
- Ormel, C. W. & Klahr, H. H. 2010, *A&A*, 520, A43
- Owen, J. E., Ercolano, B., & Clarke, C. J. 2011, *MNRAS*, 412, 13
- Paardekooper, S.-J., Baruteau, C., & Kley, W. 2011, *MNRAS*, 410, 293
- Paxton, B., Marchant, P., Schwab, J., et al. 2015, *ApJS*, 220, 15
- Pierens, A. 2015, *MNRAS*, 454, 2003
- Pierens, A. & Raymond, S. N. 2016, *MNRAS*, 462, 4130

- Pollack, J. B., Hubickyj, O., Bodenheimer, P., et al. 1996, *Icarus*, 124, 62
Rein, H. & Spiegel, D. S. 2015, *MNRAS*, 446, 1424
Rosotti, G. P., Juhasz, A., Booth, R. A., & Clarke, C. J. 2016, *MNRAS*, 459, 2790
Shakura, N. I. & Sunyaev, R. A. 1973, *A&A*, 24, 337
Shu, F., Najita, J., Ostriker, E., et al. 1994, *ApJ*, 429, 781
Suzuki, T. K., Ogihara, M., Morbidelli, A., Crida, A., & Guillot, T. 2016, *A&A*, 596, A74
Tanaka, H. & Ward, W. R. 2004, *ApJ*, 602, 388
Turner, N. J., Fromang, S., Gammie, C., et al. 2014, *Protostars and Planets VI*, 411
Vokrouhlický, D. & Nesvorný, D. 2014, *ApJ*, 791, 6

Appendix A: A convergence test for $0.1 M_{\oplus}$ embryos

We simulated a solitary embryo with the mass $M_{em} = 0.1 M_{\oplus}$, embedded in the gas/pebble disks. Practically, the setup corresponds to the simulation `embryos_0.1_120` from the main text. We used the following resolutions (in r, θ): 512×768 (very low), 1024×1536 (low), 2048×3072 (moderate), 3072×4096 (high). Per Hill sphere, it corresponds to 1.5, 3, 5, and 8 cells in the radial direction. The outcome is summarised in Figure A.1. The semimajor axis exhibits different migration rates, for very low and low resolutions, they are four to three times as large as for the moderate or high resolutions. This is due to a poor resolution of the Hill sphere, and the corotation region.

On the other hand, the eccentricity oscillations have rather similar amplitudes over the given time span (albeit the temporal evolution is somewhat undersampled). If we look at the torques in low-resolution simulations, they vary with much larger amplitudes, but on average the eccentricity seem to be sufficiently similar. The moderate and high resolutions may exhibit a long-term trend towards a larger asymptotic value.

Nevertheless, we decided to use 1024×1536 at this stage of research, because the computations would be otherwise prohibitively expensive in terms of the CPU time. We also thought the evolution may be quick enough that the high resolution actually would not be needed for the whole simulation time, if some mergers occur soon for which this resolution is sufficient.

Appendix B: Supporting figures

The supporting figures B.1 to B.3 show the simulations discussed in the main text in an alternative way.

Appendix C: Context and subsequent evolution

In order to provide a broader context for our work and expected time scales of a subsequent evolution we append a few remarks. The protoplanets we focus on in this paper (with initial masses ranging from 0.1 to $5 M_{\oplus}$) do not open a gap in the disk, and this phase is generally called a (fast) Type-I migration. Its typical time scale (at the distance of Jupiter 5.2 au) is of the order of 10 kyr, after which the radial distance changes substantially, protoplanets start to interact, etc. Only if the planetary core becomes critically massive ($\approx 20 M_{\oplus}$) it accretes and repels gas from the corotation region – possibly in mere 10^2 orbital periods – and the respective torques are zeroed (Lin & Papaloizou 1986; Crida & Morbidelli 2007; Crida & Bitsch 2017). The remaining distant spiral arms couple the planet to the disk, which is driven by the viscosity ν , and thus a (slow) Type-II migration should occur, with the time scale given by $(da/dt)_{II} = -3\nu/(2a)$, i.e. the order of 100 kyr.

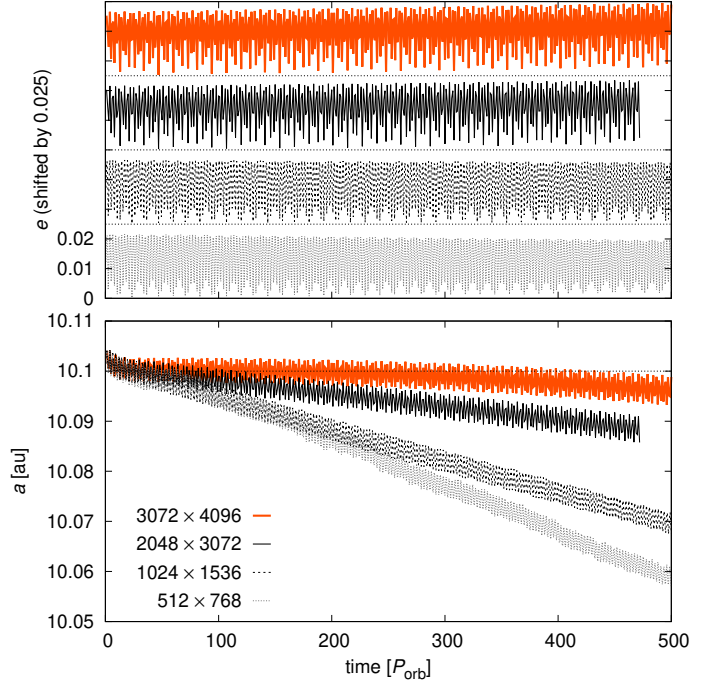


Fig. A.1. The temporal evolution of the semimajor axis (bottom) and the eccentricity (top) of a single low-mass $0.1 M_{\oplus}$ embryo embedded in the gas/pebble disks, for four different discretisations in space, namely 512×768 cells in r and θ (i.e. a very low resolution), 1024×1536 (low), 2048×3072 (moderate), and 3072×4096 (high). The amplitude eccentricity oscillations is approximately the same for all cases, even though the torques have much larger amplitudes for very low and low resolutions. To obtain a correct value for the migration rate da/dt , one would need the moderate resolution at least. The rate da/dt is about three times as large for the low resolution.

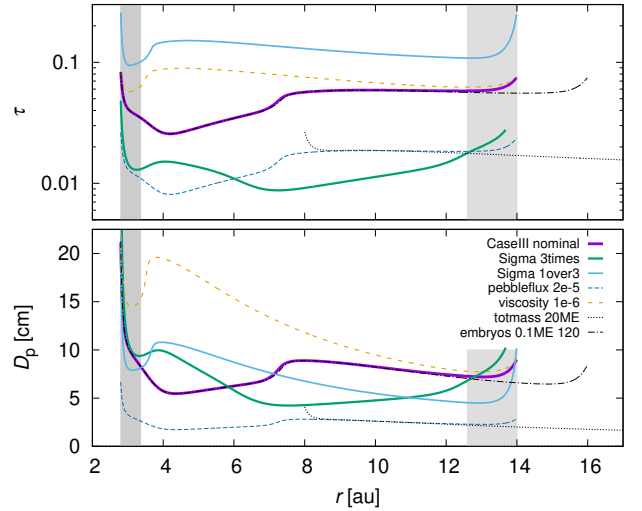


Fig. B.1. The pebble sizes D_p (top), the corresponding Stokes numbers τ (bottom) and their dependence on the radial distance r in individual simulations. The value of D_p changes in such a way to keep the pebble flux \dot{M}_p initially constant. On the other hand, the value of τ is inversely proportional to the coupling between the gas and pebbles. Both quantities are increased in the damping zones (gray strips), but this does not affect our simulation in any way.

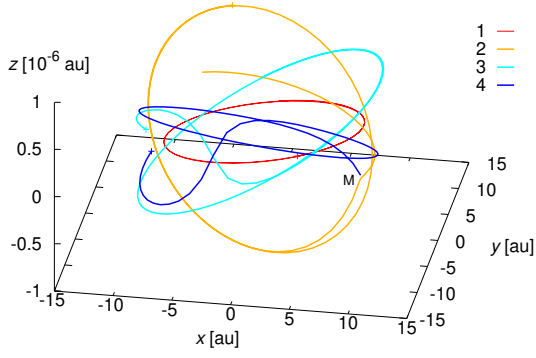


Fig. B.2. The same as Fig. 5 shown in 3D. It can be seen how the encounter proceeds in the vertical direction. Note the scale of the z coordinate is very small (10^{-6} au). The subsequent merger event is denoted by ‘M’.

While we do not study the viscous properties of the disk in any detail, we should note the (eddy) viscosity ν is actually used to describe underlying (unresolved) turbulent flows, which effectively exchange the angular momentum between differentially rotating layers. This turbulence can be driven by the vertical shearing instability VSI (a.k.a. Kelvin–Helmholtz in z direction; Nelson et al. 2013), subcritical baroclinic instability SBI (essentially, Rayleigh–Taylor with heat diffusion; Klahr & Bodenheimer 2003), magneto–rotational instability MRI (Balbus & Hawley 1991; Turner et al. 2014), although it can be suppressed in dead zones where the ionisation is too low, or spiral wave instability SWI (resonant coupling between spiral arms induced by an embedded planet and inertial-gravity waves; Bae et al. 2016). Theoretically, it is also possible that the accretion inflow is driven by a stellar wind (Günther 2013; Turner et al. 2014), if it was not weak, X-wind at the disk edge (Shu et al. 1994), or by magneto-centrifugal wind and loading of ions (Anderson et al. 2005; Suzuki et al. 2016), which all can affect the disk *surface* and carry some part of the angular momentum away.

From the observational point of view, a full disk should become pre-transitional (as defined by Espaillat et al. 2014) in the course of the outlined evolution. Transitional or even evolved disks correspond to much later phases. In the framework of young stellar object (YSO) classification, based on 2.2 to $20\ \mu\text{m}$ spectral slope of λF_λ , it corresponds to Class II objects with moderately negative slope. The above-mentioned gap opening should eliminate a part of the disk with moderate temperatures and result in a pronounced decrease of spectral-energy distribution around $\lambda \approx 10\ \mu\text{m}$.

At the same time, the central star (Sun) irradiating the disk is a pre-main sequence object of T Tauri type, for which we assume parameters $M_\star = 1 M_\odot$, $T_{\text{eff}} \doteq 4\,300\ \text{K}$, $R_\star \doteq 1.5 R_\odot$ (Paxton et al. 2015). It is usually expected the star had already low accretion rate (of the order of $10^{-8} M_\odot \text{yr}^{-1}$; Ingleby et al. 2013). In the course of stellar evolution, the convective zone recedes away from the core and only a subsurface convection remains. Most likely, a shearing zone (tachocline) is then formed which is related to an onset of the solar dynamo, an increase of the FUV, X-ray flux, and consequent photoevaporation of the disk (Owen et al. 2011). It would take another $\approx 26\ \text{Myr}$ to reach the zero-age main sequence (ZAMS). This is a typical situation for all F, G, K stars; more massive stars would be classified as Herbig Ae, Be objects.

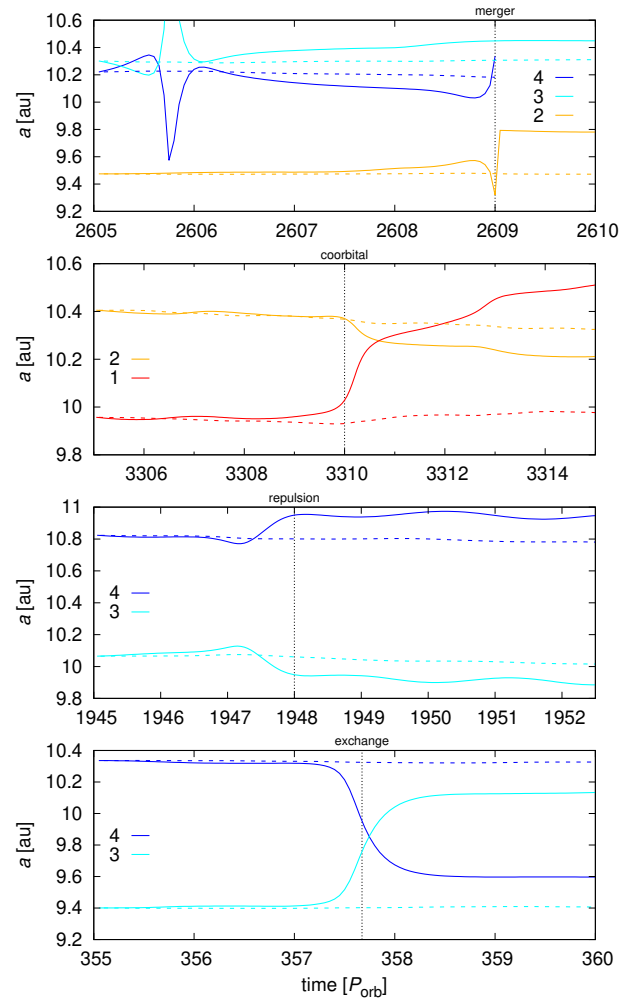


Fig. B.3. Semimajor axis $a(t)$ evolution corresponding to the torques Γ in Fig. 6. The actual orbital evolution (solid lines) of the embryos is shown together with a fictitious trajectory (dashed) obtained from the disk torques only, as an integral of the first Gauss equation, $da/dt = 2\Gamma/(rn)$, where r denotes the radial distance and n the mean motion.